Comparison of Rainfall Characteristics and Convective Properties of Monsoon Precipitation Systems over South China and the Yangtze and Huai River Basin

YALI LUO

State Key Laboratory of Severe Weather, Chinese Academy of Meteorological Sciences, Beijing, China

HUI WANG

State Key Laboratory of Severe Weather, Chinese Academy of Meteorological Sciences,
and Graduate School of the Chinese Academy of Sciences, Beijing, China

RENHE ZHANG AND WEIMIAO QIAN

State Key Laboratory of Severe Weather, Chinese Academy of Meteorological Sciences, Beijing, China

ZHENGZHAO LUO

Department of Earth and Atmospheric Sciences, and NOAA/CREST Center, City College,
City University of New York, New York, New York

(Manuscript received 22 February 2012, in final form 18 June 2012)

ABSTRACT

Rainfall characteristics and convective properties of monsoon precipitation systems over South China (SC) and the Yangtze and Huai River basin (YHRB) are investigated using multiple satellite products, surface rainfall observations, NCEP reanalysis, and weather maps. Comparisons between SC and YHRB are made for their monsoon active periods and their subseasonal variations from the premonsoon to monsoon and further to postmonsoon periods. The principal findings are as follows. (i) During the monsoon active period, region-averaged rain accumulation is greater in SC due to more frequent occurrence of precipitation systems; however, heavy rainfall contribution is greater in YHRB. These differences are related to more intense convective motion over the YHRB in association with the flatter land and more concurrent presence and stronger intensity of the low-level vortices and surface fronts. (ii) Largely in agreement with the subseasonal variations of the atmospheric thermodynamic conditions, convective intensity is enhanced progressively from the premonsoon to the monsoon and further to the postmonsoon period in both regions, as suggested by most convection proxies, except for lightning flash rate, which decreases substantially over SC but increases slightly over the YHRB from the premonsoon to the monsoon period. (iii) Compared to the monsoon active period, precipitation storms in both regions during the postmonsoon and monsoon break periods are more controlled by local instability due to solar heating but less controlled by larger-scale weather systems. This scale difference in the driving mechanisms leads to the smaller horizontal extent of the precipitation systems during the postmonsoon and monsoon break periods and also to the more pronounced afternoon peaks in precipitation system occurrence in the postmonsoon period.

1. Introduction

The Asian–Pacific summer monsoon can be demarcated into the three components shown in Fig. 1a (Ding 2007): the Indian summer monsoon (ISM), the western North Pacific summer monsoon (WNPSM), and the East Asian summer monsoon (EASM). Large-scale circulation, weather systems, and horizontal distribution of rainfall associated with the Asian–Pacific summer monsoon have been extensively studied (summary in Chang et al. 2010). However, there have been relatively few documents on storm properties, specifically convective intensity and vertical structure. Quantifying regional convective intensity and storm structure is important for many meteorological applications such as calculation of

---

Corresponding author address: Dr. Yali Luo, State Key Laboratory of Severe Weather, Chinese Academy of Meteorological Sciences, Beijing 100081, China.
E-mail: yali@cams.cma.gov.cn

DOI: 10.1175/JCLI-D-12-00100.1

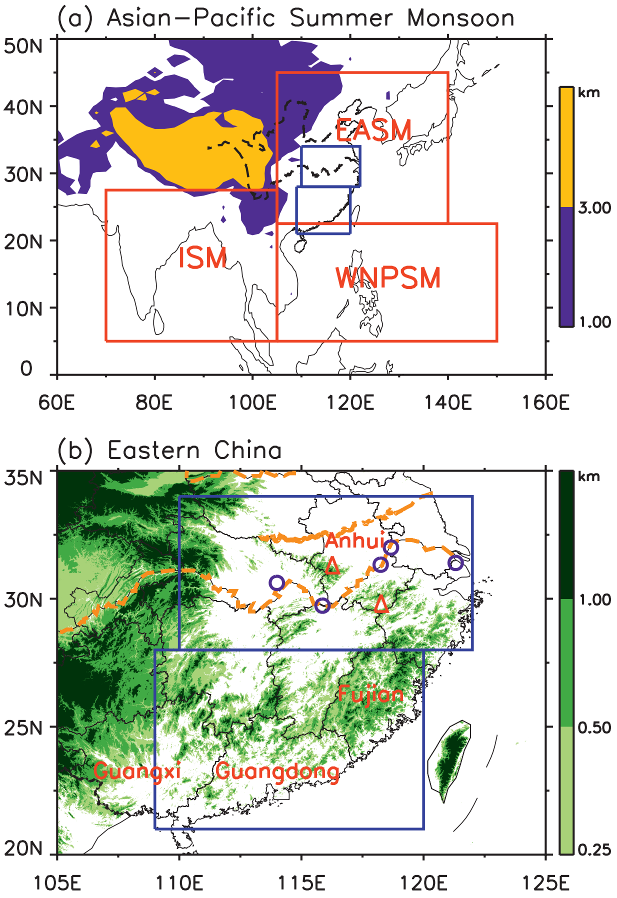

FIG. 1. (a) Locations of the three components of the Asian–Pacific summer monsoon: the East Asian summer monsoon (EASM), the Indian summer monsoon (ISM), and the western North Pacific monsoon (WNPSM). (b) Topographical map of eastern China. The locations of Yellow Mountain and Dabie Mountain are marked with red triangles and the five meteorological stations (Hankou, Jiujiang, Wuhu, Nanjing, and Shanghai) along the Yangtze River are marked by purple circles. The Yangtze, Huai, and Yellow Rivers are drawn as long dashed yellow lines, whereas province boundaries and coastal lines are represented by solid black lines in (b). Locations of provinces Guangdong, Guangxi, Fujian, and Anhui are labeled with red words. Southern China (SC) and the Yangtse–Huai River basin (YHRB) defined in the study are the land regions within the blue boxes. The elevation in (a),(b) is given by two different color bars.

the vertical profile of latent heating (Mapes and Houze 1995), physical parameterization for climate models (Arakawa 2004), and model evaluation (Varble et al. 2011).

Several studies have been conducted to characterize the joint variation of monsoon precipitation and storm properties associated with the Asian–Pacific summer monsoon circulation, using mostly multiple years of the Tropical Rainfall Measuring Mission (TRMM) (Kummerow et al. 1998) data products. Islam and Uyeda (2006) showed that in the ISM region convective intensity as represented by radar echo height decreases continuously from the premonsoon to monsoon to postmonsoon periods. Houze et al. (2007), Medina et al. (2010), and Romatschke and Houze (2011) examined the influence of the Himalayas on the ISM convection and showed systematic change in convective properties from the west to the east of the mountain range. Yuan and Qie (2008) analyzed lightning activity over the South China Sea (SCS) and found that the mean flash rate is higher during the premonsoon season than during the monsoon season, consistent with stronger vertical development of precipitation systems in the former period. Xu et al. (2009) focused on a subregion of the EASM covering southern China (SC), Taiwan, and the SCS and described the variations in rainfall and convective intensity from the premonsoon to monsoon and postmonsoon periods. Moreover, intraseasonal variations of summer monsoon rainfall over the Yangtze and Huai River basins (Fig. 1b) and the associated large-scale atmospheric circulation have been investigated (Mao and Wu 2006; Fujinami and Yasunari 2009; Yang et al. 2010).

Our present work builds upon these previous studies and further investigates rainfall characteristics and convective properties over the EASM, with the purpose to characterize the nature of cloud systems accounting for the precipitation in southeastern China. Specifically, we compare two subregions of the EASM: SC and the Yangtze–Huai River basin (YHRB). YHRB is defined as the land area within 28°–34°N, 110°–122°E, and SC as the land area within 21°–28°N, 109°–120°E (Fig. 1). SC and YHRB are usually treated separately in monsoon and mei-yu studies, especially among Chinese meteorologists, because the monsoon rain belt moves sequentially across them and the active monsoon period of the YHRB follows right after that ending in SC (Ding and Chan 2005). SC and YHRB are highly populated, accounting for nearly half of China's population and a significant share of the country's economy. It is therefore of practical importance to develop a solid understanding of the rainfall characteristics and convective properties associated with these severe weather systems. Xu et al. (2009) examined some of these aspects for SC. However, it is shown in the present study that, compared to SC, the YHRB possesses some distinct characters in precipitation and convection during the monsoon active period and in subseasonal variations of convective activity. To capture the interannual variations in the onset and ending dates of the monsoon season (e.g., Xie et al. 1998; Wang et al. 2008), we objectively define the onset and ending dates considering both rainfall and atmospheric circulation. This is in compensation to previous studies (e.g., Islam and Uyeda

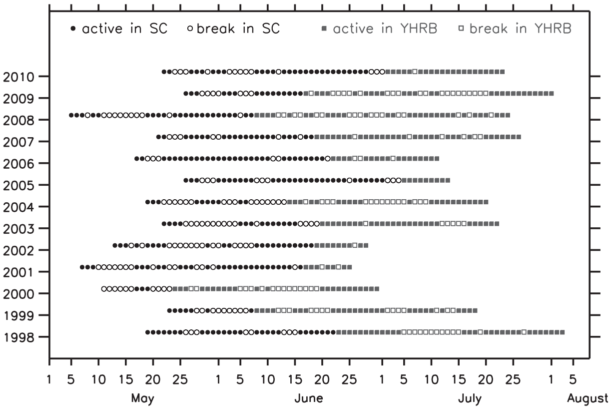

FIG. 2. Rainy and rainless days during the monsoon periods of each year in 1998–2010 over the SC (black dots or circles) and YHRB (gray squares) region: a rainy day is marked by a filled dot or square while a rainless day by a cycle or an open square.

TABLE 1. Onset and end dates of the monsoon period over the SC region and of the mei-yu period over the YHRB region in each year of 1998–2010 are shown without parentheses and brackets. Numbers in the parentheses are the numbers of days during the monsoon periods that consist of both rainy days and rainless days; the numbers in brackets are the numbers of rainy days.

Year	SC	YRHB
1998	19 May–22 Jun (35) [27]	23 Jun–3 Aug (42) [29]
1999	23 May–7 Jun (16) [7]	8 Jun –18 Jul (41) [27]
2000	11–23 May (13) [10]	24 May–30 Jun (38) [23]
2001	7 May–6 Jun (41) [27]	17–25 Jun (9) [7]
2002	13 May–18 Jun (37) [22]	19–28 Jun (10) [9]
2003	22 May–19 Jun (29) [14]	20 Jun–22 Jul (33) [27]
2004	19 May–13 Jun (26) [10]	14 Jun–20 Jul (37) [22]
2005	26 May–4 Jul (40) [30]	5–13 Jul (9) [9]
2006	17 May–21 Jun (36) [30]	22 Jun–11 Jul (20) [17]
2007	21 May–18 Jun (29) [22]	19 Jun–26 Jul (38) [32]
2008	5 May–7 Jun (34) [23]	8 Jun–24 Jul (47) [30]
2009	26 May–16 Jun (22) [15]	17 Jun–1 Aug (46) [26]
2010	22 May–1 Jul (41) [28]	2–23 Jul (22) [21]
Total	(399) [259]	(392) [279]

2006; Xu et al. 2009) in which monsoon periods were held fixed from one year to another. It is shown in section 4 that there are significant interannual variations in the onset and ending dates of the monsoon seasons over SC and the YHRB (Fig. 2; Table 1).

Another unique feature of the present study is use of multiple data sources. While TRMM products remain an important source of information in the current study, we also analyze *CloudSat*/*Cloud–Aerosol Lidar and Infrared Pathfinder Satellite Observations* (*CALIPSO*) (Stephens et al. 2002, 2008a) data, as well as ground-based precipitation measurements, reanalysis data, and weather maps. TRMM is well designed to characterize convection intensity by detecting the precipitation part of convective cloud system. *CloudSat*/*CALIPSO*, on the other hand, can capture the whole convective system, from the convective core to the stratiform precipitation region and to the nonprecipitating anvil. Luo et al. (2011) demonstrated the value of using *CloudSat*/*CALIPSO* to characterize tropical and subtropical deep convection. Hence, we borrow the analysis methods developed in Luo et al. (2011) for this study to complement TRMM. Moreover, a new gridded daily precipitation dataset based on observations from 2393 meteorological stations in mainland China is used to characterize rainfall distribution and intensity. This will further supplement previous studies using TRMM. In addition, operational objective weather-map analysis from the National Meteorological Center (NMC) of the China Meteorological Administration (CMA) is analyzed to help interpret satellite and ground-based observations. Relevant parameters include surface front, shear line of horizontal winds, and vortex at 850 hPa. Finally, reanalysis and operational analysis data are used to define the onset and end dates of the monsoon periods and compute the dynamic and thermodynamic conditions of the atmosphere. The use of multiple data sources offers different but complementary perspectives on the convective systems and their environment, leading to a more complete depiction of the phenomena studied.

The remainder of the paper is organized as follows: Sections 2 and 3 describe the data and methodology, respectively. Onset and end dates of the monsoon periods are given in section 4. Section 5 compares precipitation systems over SC and the YHRB during their monsoon active periods. Contrasting of the monsoon period to the pre- and postmonsoon periods in SC and the YHRB is presented in sections 6 and 7, respectively. This article ends with a summary in section 8.

2. Data

In the present study, the following datasets are utilized to investigate rainfall characteristics and convective properties of precipitation systems over the SC and YHRB regions: 1) a new ground-based gridded daily precipitation data product, 2) the University of Utah TRMM-based precipitation feature (PF) dataset, 3) the *CloudSat*/*CALIPSO* data products, 4) the U.S. National Centers for Environmental Prediction (NCEP) reanalysis data, and 5) the weather maps produced by the CMA NMC. All datasets cover the years from 1998 to 2010 unless otherwise stated. This section only provides some essential facts about the datasets, together with references. Section 3 will explain in more detail how different datasets are used.

a. *Gridded daily precipitation dataset*

The daily precipitation dataset with a resolution of 0.25° by 0.25° is used in the determination of the monsoon periods of each year and also in the analysis of surface rainfall characteristics. The dataset was developed at the CMA Chinese Academy of Meteorological Sciences based on precipitation observations at 2393 meteorological stations in mainland China. This number of meteorological stations is significantly larger than those used in previous studies on precipitation over mainland China [e.g., 588 stations used by Yu et al. (2007)]. The observations at the individual stations are interpolated to a grid that nearly completely covers the entire mainland China using a mixed interpolation method (J.-L. Hu et al. 2008) that combines the Barnes scheme (Barnes 1964) and the precipitation frequency of the closest station (Shen et al. 2001, 2005). The gridded daily precipitation was assessed through cross-validation statistics and was found to be close to the observations in terms of variation and frequency of precipitation (J.-L. Hu et al. 2008). This new dataset is for the first time applied here to study statistics of the SC/YHRB precipitation systems.

b. *TRMM data*

The University of Utah TRMM level-1 cloud and precipitation feature database is utilized in this study to analyze structure characteristics and convective properties of precipitation systems. This dataset was developed by Liu et al. (2008a) through collocation of the multiple observations from four different instruments aboard the TRMM satellite: precipitation radar (PR), TRMM Microwave Imager (TMI), visible and infrared scanner (VIRS), and lightning imaging sensor (LIS). More details about this dataset may be found in Liu (2007). Section 3b will explain in detail how precipitation features are constructed and analyzed to characterize convective properties.

c. CloudSat/CALIPSO *data*

Two *CloudSat* standard data products, publicly available as the level-2 2B Geometrical Profiling Product (2B-GEOPROF) (Mace et al. 2007) and 2B-GEOPROF-lidar (a combination of *CloudSat* and *CALIPSO*), are used to study properties of deep convective clouds. Detailed information about the *CloudSat* products may be found in the *CloudSat* standard data products handbook (available at http://cloudsat.cira.colostate.edu/). These data are collocated at the spatial grid of the cloud profiling radar (CPR) aboard *CloudSat* with resolutions of 2.5 km along track by 1.4 km across track and 240 m in the vertical. The data from June 2006 to 2010 are utilized.

d. *NCEP datasets*

Two kinds of NCEP datasets, the NCEP–National Center for Atmospheric Research (NCAR) reanalysis data (Kalnay et al. 1996) and NCEP Global Forecast System Final (FNL) Operational Global Analysis data, are used in this study. The NCEP–NCAR reanalysis data with 2.5° resolution are used in the determination of the starting and ending dates of the monsoon periods, while the FNL data available at 1° resolution during 2001–10 are used to reveal the dynamic and thermodynamic conditions of the atmosphere.

e. *Weather maps*

The operational objective weather-map analysis made at the CMA NMC is used to determine presence of relevant weather systems. The maps of the weather analysis on the ground surface are available four times per day (at 0000, 0600, 1200, 1800 UTC), and those on the isobaric surfaces (850, 700, and 500 hPa) are available twice per day (at 0000 and 1200 UTC).

3. Methodology

a. *Determination of the SC/YHRB monsoon periods*

To determine the onset and ending dates of the monsoon periods in the SC and YHRB regions, we consider not only the intensity, horizontal extent, and continuity of surface precipitation over the regions but also the subseasonal variation of the East Asia atmospheric circulation. For each region, we first define ''rainy day'' as a day that satisfies two criteria (Y.-M. Hu et al. 2008; Hu and Ding 2010): (i) more than one-third of the grids over the whole region have precipitation (>0.1 mm) and (ii) the total daily rainfall amount over the region is more than half of the climatologically averaged (over 1971–2010) rainfall amount during June and July for YHRB or May and June for SC. A day that is not determined as a rainy day is then defined as ''rainless day.''

The SC monsoon period starts along with the onset of the SCS summer monsoon (Ding and Chan 2005), which is determined following the CMA National Climate Center (NCC) (http://cmdp.ncc.cma.gov.cn/Monitoring/monsoon.htm). It is the date when the 850-hPa zonal wind stably changes from easterly to westerly and the 850-hPa potential pseudoequivalent temperature become greater than 340 K over the SCS area (10°–20°N, 110°–120°E). The end date of the SC monsoon period is determined as the day before the starting date of the monsoon period in YHRB (i.e., the mei-yu period). During the mei-yu period the ridge line of the western Pacific subtropical high must be located between latitudes 19° and 26°N. The mei-yu season starts when the first rainy day occurs in the YHRB region. It ends when the following two criteria are satisfied continuously for more than five days: (i) the ridge of the western Pacific subtropical high exceeds 26°N and (ii) surface air temperature at more than one-third of the grids over the whole YHRB region surpasses 35°C (Y.-M. Hu et al. 2008).

The monsoon period of each year in each region is further divided into active and break periods that consist of the rainy days and rainless days, respectively. The pre- and postmonsoon periods each cover one continuous month. The end date of the premonsoon period is the first day that is a week before the starting date of the monsoon period. The starting date of the postmonsoon period is the first day that is a week after the ending date of the monsoon period. A week interval between the monsoon period and the pre- or postmonsoon period is meant to exclude the ambiguous period between them.

b. *Definition and classification of precipitation features and interpretation of some precipitation feature parameters from TRMM*

To effectively summarize the huge orbital pixel-level observations from TRMM, we employ a precipitation-event-based analysis method following previous studies of, for example, Nesbitt et al. (2000) and Liu et al. (2008a). A precipitation feature (PF) is defined as a contiguous area consisting of the TRMM 2A25 (Iguchi et al. 2000) near-surface raining pixels. The PFs over the analysis regions are categorized into mesoscale convective system (MCS), sub-MCS, and other, based on the PF area and existence of convective pixel in the PF (Xu et al. 2009). The criterion of a convective pixel is based on the TRMM 2A23 product (Awaka et al. 1998). If there is no convective pixel in a PF, the PF is categorized into the other type, which may be part of a decayed convective system or stratiform system. If a PF has at least one convective pixel and its area larger than 1000 km^2, it is considered as an MCS-type PF; otherwise, it is a sub-MCS-type PF.

Parameters that represent the size, near-surface rainfall, radar reflectivity, passive microwave brightness temperatures, and flashes of a PF are used to describe precipitation properties. The area of a PF measures the horizontal extent of a contiguous precipitation region. The near-surface volumetric rain of a PF is the sum of near-surface rainfall over all pixels within the PF, which combines the effects of rainfall intensity and the areal extent of the PF. The maximum radar reflectivity at 6 km (maxdbz_6km) is defined as the largest reflectivity value at 6 km above the mean sea level in a PF. The maximum height of the 30-dBZ echo (maxht_30dBZ) is defined as the highest altitude that the 30-dBZ echo reaches. The minimum polarization-corrected brightness temperature at 85 GHz (min85PCT) is determined by the optical path of large ice particles at 85 GHz (Cecil et al. 2002, 2005). The flash count is the sum of flash events in a PF, and the flash rate is the flash count divided by the mean view time of the PF. Among these PF parameters, the maxdbz_6km, maxht_30dBZ, min85PCT, and flash rate are good proxies of convective intensity of the PFs (e.g., Zipser and Lutz 1994; Nesbitt et al. 2000; Zipser et al. 2006). Moreover, vertical profile of radar reflectivity (VPRR), defined as maximum radar reflectivity of a precipitation system as a function of height, is also a strong indicator of storm intensity and lightning probability (Zipser and Lutz 1994).

c. *Analyses of deep convection seen by* CloudSat/CALIPSO

Deep convective cores (DCCs) and deep convective systems (DCSs) seen by *CloudSat* are defined following Luo et al. (2011). A DCC is defined as a *CloudSat* profile that satisfies the following two criteria: 1) it contains continuous radar echo from cloud top to near the surface (i.e., the distance between the cloud-layer bottom and the ground surface is <3 km) and 2) the top of the cloud layer (which corresponds to the top of the echo of about −30 dBZ) and the maximum height of the 0-dBZ echo and the 10-dBZ echo detected by the *CloudSat* CPR are located above 12, 11, and 9 km, respectively. A DCS is then defined as a contiguous region (i.e., vertical cross section) consisting of cloudy radar profiles that contain at least one DCC with the noncore cloudy profiles either having cloud tops above 10 km or maximum reflectivity greater than 10 dBZ. Using this definition, cirrus and anvil clouds as well as shallow precipitating clouds that are connected to the deep convective core are considered as inherent parts of a DCS.

We then perform two analyses. First, to examine the internal vertical structure of the DCCs, we analyze statistics of the following parameters (Luo et al. 2011): 1) cloud-top heights (CTHs) seen by *CALIPSO* lidar (CTH_lidar) and *CloudSat* CPR (CTH_CPR) and 2) echo top heights[1] (ETHs; the maximum heights reached by the 0- and 10-dBZ CPR echoes, referred to as H_0dBZ and H_10dBZ, respectively). Second, we analyze the horizontal span of the DCSs and fractional

---

[1] *CloudSat* is a millimeter-wavelength radar, and 10–15 dBZ is about as large as it can get. Our correlation study suggests that 10 dBZ from *CloudSat* corresponds approximately to 20 dBZ from TRMM.

contributions of anvils and DCC to the DCSs. Anvils are defined as part of a DCS that has cloud base above 5 km.

d. Analyses of dynamic and thermodynamic conditions and weather systems

To better understand the rainfall characteristics and convective properties of the precipitation systems, dynamic and thermodynamic conditions of the atmosphere as well as occurrence and intensity of major weather systems are examined. Five parameters calculated from the NCEP FNL data that are relevant to development of convection [namely, relative vorticity, meridional gradient of equivalent potential temperature $\partial\theta_e/\partial y$, vertical velocity of air motion ω, convective available potential energy (CAPE), and total precipitable water (TPW)] are selected. The weather maps provided by the CMA NMC are used to determine the presence of surface front, shear line of horizontal winds, and vortex at 850 hPa.

4. Onset and end dates of the monsoon periods

The onset and end dates of the SC monsoon period and the the YHRB mei-yu period during each year of 1998–2010 from our analysis are shown in Table 1 and Fig. 2. The earliest onset (end) date of the SC monsoon period is 5 May (23 May) and the latest is 26 May (4 July). The earliest end date of the YHRB mei-yu period is 25 June and the latest is 3 August. The monsoon periods in SC and YHRB cover 399 and 392 days, respectively, in total during the 13 years. The monsoon active period over SC (YHRB) consists of 259 (279) days, accounting for 65% (71%) of the entire monsoon period. The duration varies year by year. During 1998–2010, the shortest is 13 (9) days and longest is 41 (47) days in SC (YHRB). The average duration of the SC monsoon season is approximately 31 days, which is comparable to Chen (1988) and about 14 days shorter than the one defined by Xu et al. (2009). Note that the SC monsoon season is held fixed from 11 May to 24 June for all years in Xu et al. (2009). The average duration of the YHRB mei-yu season is 30 days.

The mei-yu onset and end dates obtained here are largely consistent with previous studies. For example, Ding et al. (2001) and Ding and Liu (2001) stated that the 1998 mei-yu consists of two periods: 28 June–3 July and 17 July–early August. Jin et al. (2006) indicated that 20 June–22 July is the rich rainy season over the YHRB during 2003. These are nearly the same as our results. Compared to the mei-yu periods defined by the CMA NCC (Zhao 1999), our mei-yu periods are almost the same for the years 1998, 2001, 2005, and 2006. However, for the years 1999, 2003, 2004, 2007, 2008, and 2010 the mei-yu end dates obtained in this study are later than those of CMA NCC. Moreover, ‘‘no occurrence of mei-yu’’ (i.e., ‘‘empty mei-yu’’) is defined by CMA NCC for the years 2000, 2002, and 2009 while our analysis produces 23, 9, and 26 days of the mei-yu rainy period, respectively. Sun et al. (2005) can lend some support to our result of 2000: they found a mei-yu front system near Dabie Mountain (Fig. 1b; located between Yangtze River and Huai River) during 20–22 June 2000, which is part of our mei-yu season. Further, Liang and Ding (2011) pointed out that the CMA NCC incorrectly defined 2009 as a year of empty mei-yu and the period from late July to early August is the mei-yu season of 2009. In general, the reason for the differences between this study and the CMA NCC probably lie in that we define the mei-yu period by considering precipitation over the entire YHRB region, whereas NCC CMA used precipitation at only five stations along the middle and lower reaches of the Yangtze River (locations of the stations are shown in Fig. 1b).

TABLE 2. Statistics during the monsoon periods of 1998–2010 in SC and the YHRB.

	SC	YHRB
Fraction of rainbands having a horizontal inclination smaller than 30°	78%	81%
Mean lifetime of monsoon rainbands	5 days	5 days
Fraction of rainfall accumulation from the monsoon active periods	95%	95%

5. Comparison between the SC and YHRB monsoon precipitation

a. Daily rainbands and rainfall accumulation

This section covers analysis of the gridded daily precipitation dataset based on station observations. A wide range of bandlike precipitation region (i.e., rainband) is found almost every day during the SC or YHRB monsoon active period. The rainbands are mostly quasi-west–east oriented, with 78% (SC) and 81% (YHRB) having a horizontal inclination smaller than 30° (Table 2), reflecting the well-known quasi-west–east orientation of the monsoon rainbands (e.g., Ding 2007). The mean lifetime of the monsoon rainbands is 5 days in both regions, indicating the persistent nature of the precipitation events. About 95% of the rainfall accumulation in the entire monsoon periods of 1998–2010 occurs in the monsoon active periods over both regions. In contrast to the extensive and persistent rainbands during

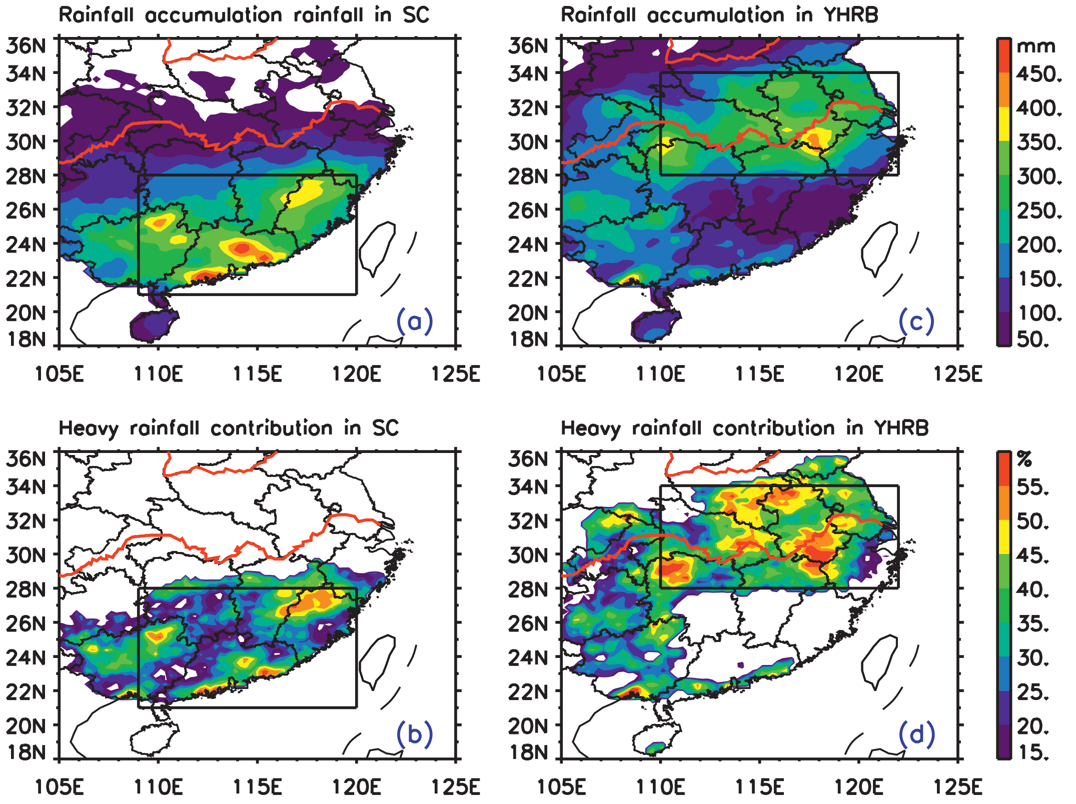

FIG. 3. (top) The averaged rainfall accumulation in the monsoon active period of 1998–2010 in the (a) SC and (c) YHRB region. (bottom) The contribution from heavy rainfall (>50 mm day^{-1}) to the rainfall accumulation corresponding to upper panels, but only locations with the rainfall accumulation larger than 150 mm are shown. These results are produced from the gridded daily precipitation dataset based on station observations.

the monsoon active periods, precipitation in the monsoon break periods tends to be of smaller temporal and spatial scales.

Figure 3 shows geographical distributions of the rainfall accumulation and heavy rainfall (>50 mm day^{-1}) contribution during the monsoon periods. Note that the YHRB monsoon period is defined as right after the SC monsoon period, so Figs. 3a,c refer to two different but consecutive periods (see Fig. 2). They clearly show that rainfall centers move from SC to YHRB, supporting our definitions of the SC and YHRB monsoon periods (section 3a). During the SC monsoon period, there are three major rainfall maxima or "hot spots" exceeding 400 mm per season located at coastal and inner Guangdong and northeastern Guangxi. In the YHRB region, there is only one mei-yu rainfall maximum exceeding 400 mm per season located at southern Anhui. These rainfall centers are contributed significantly (>50%) by heavy rainfall (Figs. 3b,d), which is probably related to the topographical features over the regions (Fig. 1b), such as the mountains scattered in Guangdong, the trumpet-shaped topography over northeastern Guangxi, the Yellow Mountains at southern Anhui, and the Dabie Mountains at southwestern Anhui. These features of the underlying surface can enhance development of convection and influence intensity and location of rainfall (e.g., Zhao et al. 2008).

Table 3 provides a concise summary of the rainfall characteristics over SC and YHRB. The region-averaged rainfall accumulation is larger in SC (284 mm per season) than YHRB (252 mm per season). The fraction of area with rain accumulation >360 mm per season is also larger in SC (12.7%) than in YHRB (3.3%). The larger amount of rainfall accumulation in the SC region is caused by more frequent occurrences of precipitation systems, as suggested by occurrence frequency of the TRMM PFs (section 5b). However, rainfall accumulation in the YHRB region sees a larger contribution from heavy rain than the SC region (38% versus 30%) and a larger fraction of area with heavy rainfall contribution >50% (14.9% versus 7.0%), suggesting possible differences in convective intensity between the two regions. Section 5b examines TRMM data to further answer the question pertaining to the contrast in occurrence and convective properties of precipitation systems between the SC and YHRB regions.

TABLE 3. Region-averaged rain accumulation (mm per season), region-averaged contribution (%) by heavy rainfall (>50 mm day^{-1}), areal fraction (%) with rain accumulation larger than 360 mm per season, and areal fraction (%) with heavy rainfall contribution larger than 50%, during the premonsoon, monsoon active, and postmonsoon periods of 1998–2010 in the SC and YHRB regions.

Characteristic	pre	active	post
SC			
Rainfall accumulation (mm)	203	284	223
Heavy rainfall contribution (%)	19	30	29
Areal fraction (%) with accumulation > 360 mm per season	0	12.7	2.9
Areal fraction (%) with heavy rainfall contribution > 50%	1.1	7.0	2.3
YHRB			
Rainfall accumulation (mm)	135	252	154
Heavy rainfall contribution (%)	21	38	20
Areal fraction with accumulation > 360 mm per season (%)	0	3.3	0
Areal fraction with heavy rainfall contribution > 50%	0.2	14.9	0.3

TABLE 4. Total population (P) and near-surface volumetric rainfall (R) (10^7 mm h^{-1} km^2) of all precipitation features (PFs) and the relative percentages from the three PF types (MCS, sub-MCS, and other) during the premonsoon, monsoon active, monsoon break, and postmonsoon periods of 1998–2010 in the southern China (SC) region. The averaged areas (km^2) of the MCS-type PFs are also shown.

	Total PFs		MCS (%)			Sub-MCS (%)		Other (%)	
Period	P	R	P	R	Area (km^2)	P	R	P	R
pre	18 794	2.65	3.5	86.8	9233	27.4	9.6	69.1	3.6
active	18 376	2.85	3.7	88.2	11 138	32.6	7.9	63.7	3.9
break	4972	0.49	2.8	78.8	8189	37.7	15.6	59.5	5.6
post	22 741	2.90	3.8	80.3	6920	46.6	16.8	49.6	2.9

b. *Properties of TRMM PF*

A total of 18 376 and 28 014 PFs are found in SC and YHRB during their monsoon active periods of 1998–2010 (Tables 4, 5). The larger PF population in the YHRB region is mainly due to the TRMM latitudinal sampling bias; that is, TRMM has a higher sampling frequency near 35°N and 35°S compared with lower latitudes. A few similarities can be seen between the two regions in terms of population and rainfall contribution of the three types of PFs: First, the MCS-type PFs account for only 3%–4% of the total PF populations, but they contribute to approximately 90% of the total near-surface rainfall. Second, a significant fraction of the PFs (i.e., 64% in SC and 75% in YHRB) are nonconvective that produce only 3%–4% of the total rainfall.

As the MCS-type PFs are the dominant rainfall producer, their convective intensity is compared between the two regions. Four proxies of convective intensity (maxdbz_6km, maxht_30dBZ, min85PCT, and flash rate) show consistent signals: namely, the YHRB region has larger maxdbz_6km, higher maxht_30dBZ, lower min85PCT, and greater flash rate (Fig. 4), confirmed to be statistically significant at 99% confidence limit by Student's t tests. Collectively, they suggest that the precipitation systems in the YHRB contain stronger convective motion than SC. Comparisons of the cumulative distributions of VPRR for both MCS- and sub-MCS-type PF categories between the two regions during the monsoon active periods (Fig. 5) also clearly show that the monsoon convection is more intense over the YHRB region than the SC region as more larger radar echoes extend to greater altitudes over YHRB.

In spite of their relatively weaker convective intensity, the SC monsoon storms occur substantially more frequently than their counterparts over theYHRB (Fig. 6), resulting in larger rainfall accumulation in SC (Fig. 3a versus Fig. 3c; Table 3). The convective storms (the MCS and sub-MCS PFs) occur most frequently in the Guangdong and Guangxi provinces (Figs. 6a,b), corresponding to the distinct maxima of rainfall accumulation over SC (Fig. 3a). Interestingly, the nonconvective systems occur most frequently in northwestern Fujian (Fig. 6c), also corresponding to the secondary maximum rainfall accumulation there (Fig. 3a). These results suggest that the underlying mechanisms governing formation and evolution of precipitation systems at northwestern Fujian probably differ from those at Guangdong and Guangxi. The mountains in northwestern Fujian may not favor the formation and maintenance of convection during the monsoon active period of SC.

c. *Structure of deep convective systems from* CloudSat/CALIPSO

In total, 21 and 40 DCSs were seen by the *CloudSat*/*CALIPSO* in SC and YHRB, respectively, during their monsoon active periods of 2006–10 (Table 6). From the total number of DCS pixels, we can estimate the average

TABLE 5. As in Table 4, but over the YHRB region during the pre-mei-yu, mei-yu active, mei-yu break, and post-mei-yu periods.

	Total PFs		MCS (%)			Sub-MCS (%)		Other (%)	
Period	P	R	P	R	Area (km^2)	P	R	P	R
pre	26 225	2.48	2.3	87.5	14 047	14.8	5.9	82.9	6.6
active	28 014	5.13	3.5	91.1	13 251	21.3	5.7	75.2	3.2
break	7642	0.70	2.9	81.7	8178	20.9	13.2	76.2	5.1
post	31 660	3.75	3.3	80.0	7864	33.9	16.3	62.8	3.7

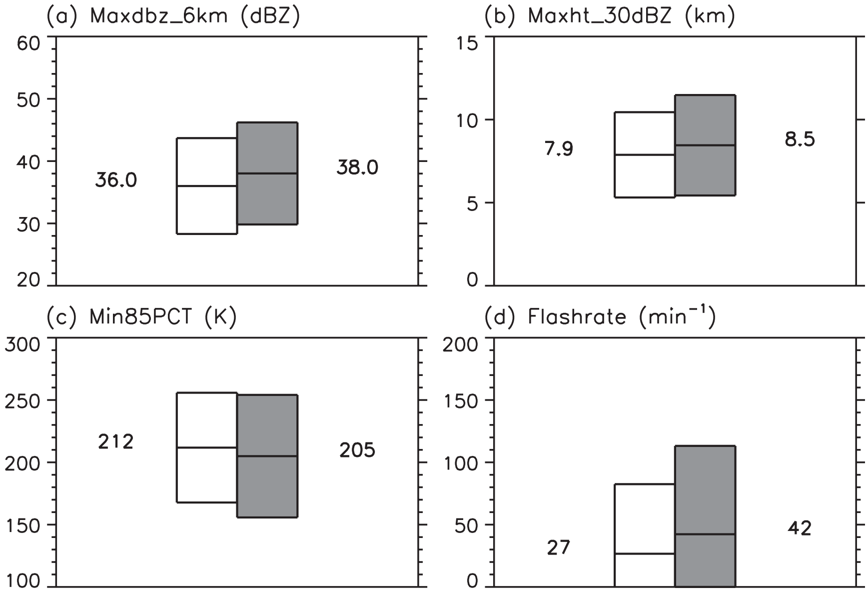

FIG. 4. Proxies of convection intensity of the MCS-type precipitation features (PFs) in SC (white bars) and the YHRB (gray bars) during their monsoon active periods. The middle of each bar represents the mean and the top (bottom) of each bar indicates the mean plus (minus) the standard deviation. Numbers in each panel represent the mean values for the indicated variables.

horizontal span (or size) of the DCSs, which is about 279 km in SC and 176 km in YHRB. However, the fraction of DCC out of the whole DCS is 16.9% in YHRB, nearly twice of that in SC (8.2%). It follows that the average DCC coverage within a DCS is larger in YHRB (30 km) than in SC (23 km). Hence, the composite picture emerging out of the *CloudSat/CALIPSO* analysis is that DCSs in SC are on average 58% larger than the YHRB counterpart but the embedded DCCs are 36% smaller. These DCS structural differences are closely related to the contrasting precipitation characteristics between the two regions: namely, larger rainfall coverage over SC but more heavy rain contribution over YHRB. In the vertical dimension, CTH and ETH of the DCCs are very similar between the two regions (Fig. 11).

Since *CloudSat* and *CALIPSO* also detect the attached anvil clouds (which TRMM misses for the most part), we calculate the statistics for the anvil fraction. It does not differ significantly between the two regions: 56.5% (SC) and 52.3% (YHRB). However, considering DCS size is larger in SC than in YHRB by 58%, anvil coverage is more extensive in SC by a similar amount. Although not directly contributing to the surface rainfall, cirrus anvil spawning out of deep convection produces significant radiative heating, which affects large-scale circulation that, in turn, influences convection development and rainfall production (e.g., Stephens et al. 2008b). These radiative feedbacks are beyond the scope of the current study but certainly warrant further investigations.

d. Environmental conditions and weather systems

Why do the convective precipitation systems occur more frequently but exhibit weaker convective intensity in SC than in the YHRB during the monsoon active periods? Differences in topographic features, atmospheric environment, and the associated weather systems may contain some clues (e.g., Ninomiya 2004; Ninomiya and Shibagaki 2007). The land area of SC has mountainous regions facing the ocean, while in the YHRB large areas are covered by rather flat land except for areas around Yellow Mountain and Dabie Mountain (Fig. 1b). Southwesterlies blow into the two regions in each monsoon active period (Figs. 12b and 13b), carrying abundant moisture from the ocean. Under such conditions, orographic lifting or thermally driven local circulation frequently occurs around the mountainous regions of SC but rainfall intensity may not be strong because the heights of mountains in SC are not so high. In contrast, due to the flatness, large-scale low-level convergence in association with surface front and mesoscale vortex features are needed to enhance convective storms over the YHRB. Therefore, the occurrence frequency decreases but the intensity increases in YHRB.

Our analyses confirm that the YHRB monsoon precipitation is in association with more frequent occurrence and stronger intensity of surface fronts and low-level

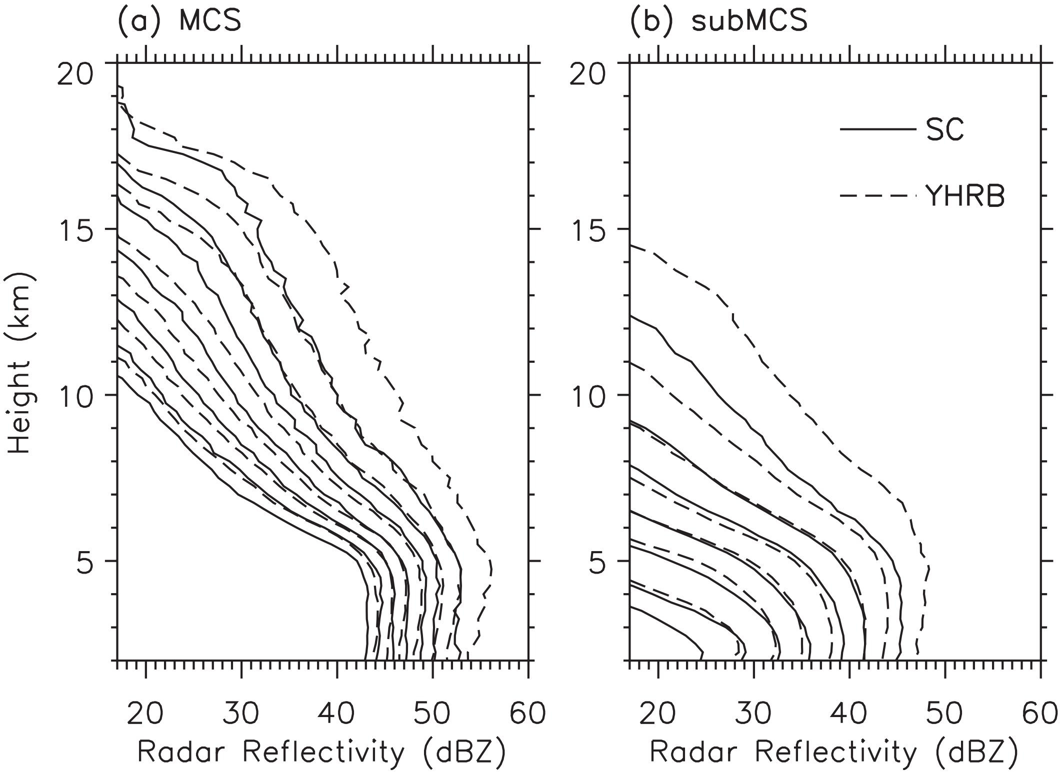

FIG. 5. Cumulative distributions of vertical profiles of maximum radar reflectivity (from bottom to top: in 50th, 60th, 70th, 80th, 90th, 95th, and 99th percentiles) for the MCS- and sub-MCS-type PFs during the monsoon active periods of 1998–2010 over SC (solid lines) and the YHRB (dashed lines).

vortices than the SC. Occurrence frequencies of major weather systems (i.e., surface front, shear line of horizontal winds, and vortex at 850 hPa) are summarized for the MCS-type PFs seen by TRMM (Table 7). Front intensity is estimated using the minimum value of meridional gradient of equivalent potential temperature, $\partial\theta_e/\partial y$ (which is negative as θ_e decreases toward the north), near the surface and at the 850-hPa level. As the results are qualitatively consistent with each other, only the 850-hPa results are shown (Fig. 7c). Vortex intensity is estimated using maximum relative vorticity at the 850-hPa level. The means and standard deviations of the intensity estimates are provided in Figs. 7c,d. While previous studies mentioned the link between these weather systems and monsoon rainfall production (Ding et al. 2011), our analysis represents the first time such analysis is conducted in a quantitative way. Table 7 shows that surface fronts were present about 66% (72%) of the times when TRMM observed the MCS-type PFs in the SC (YHRB) region. The percentages increase to 91% over both regions if the presence of an 850-hPa shear line is included. Fronts in the YHRB on average are stronger than those in SC: the mean values of minimum $\partial\theta_e/\partial y$ on the 850-hPa level are -5.8 K $(100\ \mathrm{km})^{-1}$ (YHRB) and -4.6 K $(100\ \mathrm{km})^{-1}$ (SC). Low-level vortices were present 38% (YHRB) and 19% (SC) of the time. Many of the low-level vortices formed locally in the regions, mostly on a shear line of horizontal winds. Some of the YHRB low-level vortices are in association with vortices that form over the Tibetan Plateau and move eastward out of the plateau (Yasunari and Miwa 2006; Fujinami and Yasunari 2009), possibly influenced by interactions among environmental airflow, internal circulation of the vortices, and diabatic heating (Li et al. 2011). Low-level vortices in the YHRB are also stronger than in SC: the means of maximal relative vorticity are $11.1 \times 10^{-5}\ \mathrm{s}^{-1}$ (YHRB) versus $9.6 \times 10^{-5}\ \mathrm{s}^{-1}$ (SC).

Another explanation of the stronger (weaker) convection intensity in YHRB (SC) could be traced to the well-known contrast between oceanic and continental convection: that is, oceanic convection is usually larger in size, occurs more frequently, and contains more total rainfall but is weaker in intensity (Zipser et al. 2006). The YHRB is located farther inland than SC and thus YHRB convective storms are more continental in nature compared to the counterparts over SC.

Cumulative frequency distributions of ω (not shown) appear similar in SC and YHRB. The domain- and

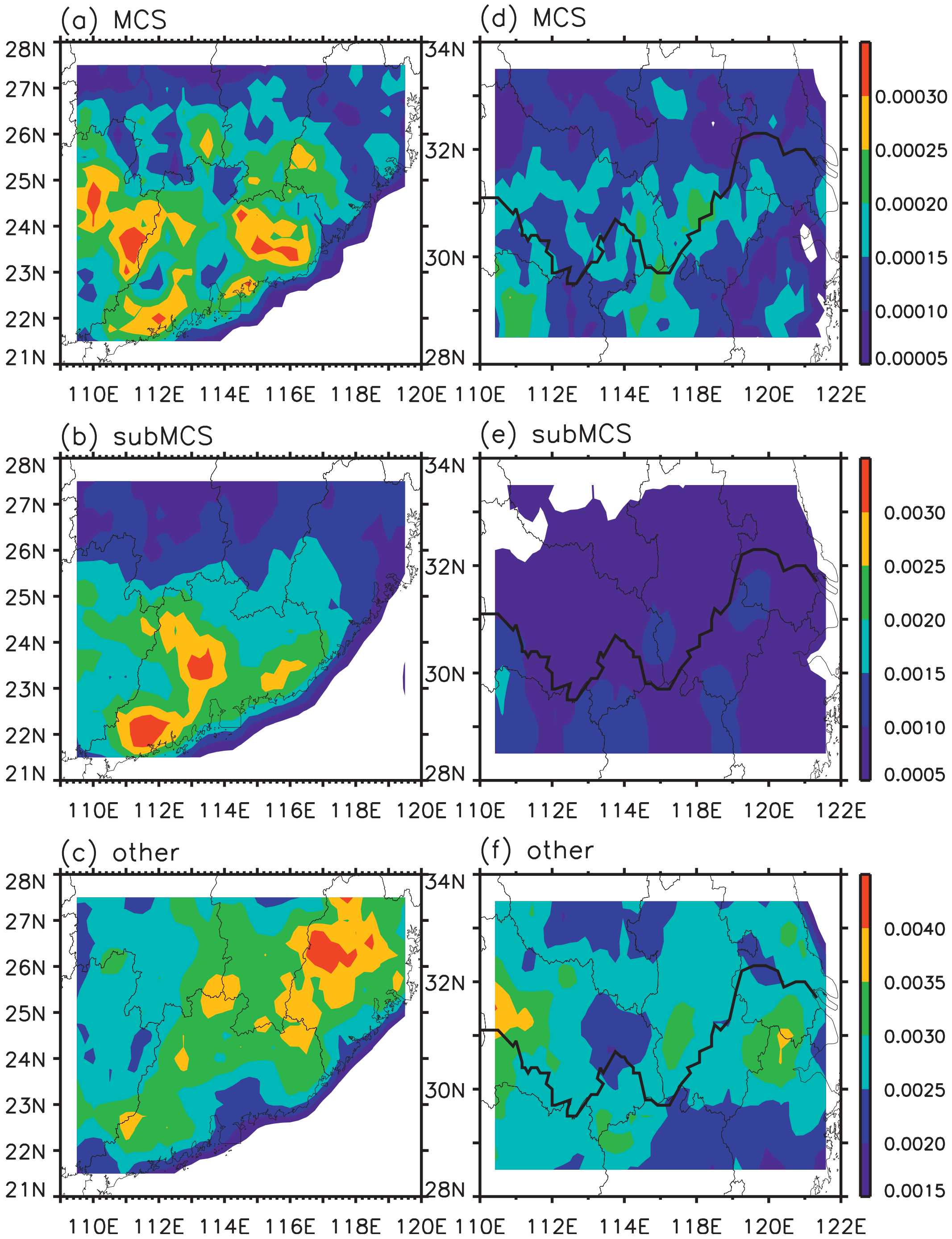

FIG. 6. Geographical distributions of occurrence frequency of the three PF categories (MCS, sub-MCS, and other) in the monsoon active periods of 1998–2010 over (a)–(c) SC and (d)–(f) YHRB. The number of PF in each 1° by 1° box is divided by the number of the TRMM PR pixels in the box to remove TRMM's latitudinal sampling bias.

time-averaged values of CAPE and TPW are also close in SC and YHRB: 637 J kg^{-1} versus 627 J kg^{-1} and 53 mm versus 52 mm (Fig. 7). These results suggest that the statistics of ω, CAPE, and TPW are essentially comparable between SC and YHRB during their monsoon active periods, although low-level vortices and fronts in the YHRB are stronger than over SC.

To better understand factors that determine convective intensity, it is desirable to investigate the detailed physical processes at cloud scale and mesoscale during

TABLE 6. Statistics of *CloudSat* deep convective systems (DCSs) in SC and YHRB during their premonsoon, monsoon active, and postmonsoon periods of 2006–10: total number of DCSs, total number of pixels in the DCSs, mean DCS size (km), mean anvil size (km) and anvil fraction (%) out of the whole DCSs, and mean size (km) of DCC and DCC fraction (%) out of the DCSs. Results during the monsoon break period are not shown because of too few samples of DCSs (4 in SC and 7 in YHRB).

Period	Total DCS	Tot pixel in DCS	Mean DCS Size	Mean size and fraction of anvil	Mean size and fraction of DCC
			SC		
pre	12	1702	156	66 (42.5)	16 (10.5)
active	21	5318	279	157 (56.5)	23 (8.2)
post	39	8682	245	140 (57.0)	38 (15.5)
			YHRB		
pre	12	5614	515	206 (40.1)	36 (7.0)
active	40	6397	176	92 (52.3)	30 (16.9)
post	40	5789	159	78 (48.9)	19 (12.0)

the life cycle of precipitation systems. This could be achieved through a combination of ground radar observations and successful high-resolution numerical simulations (e.g., Luo et al. 2010). However, this is beyond the scope of the present study and will be pursued in the future.

TABLE 7. Occurrence frequency (%) of three types of weather systems, that is, surface front, shear line of horizontal winds at 850 hPa, and vortex at 850 hPa, when TRMM observed the MCS-type PFs in the SC and YHRB regions during the years 2001–10.

Weather system	pre	active	break	post
	SC			
Surface front	46	66	32	30
Surface front and/or 850-hPa shear line	72	91	52	47
850-hPa vortex	11	19	7	10
	YHRB			
Surface front	63	72	52	45
Surface front and/or 850-hPa shear line	82	91	70	64
850-hPa vortex	36	38	14	17

6. Contrasting monsoon to pre- and postmonsoon periods in South China

a. Properties of surface rainfall and TRMM PF

Amounts of rainfall accumulation at the surface and the corresponding contribution from heavy rainfall (>50 mm day^{-1}) differ among the periods of the monsoon (Table 3). The amount of rainfall accumulation in the SC region is largest during the monsoon active

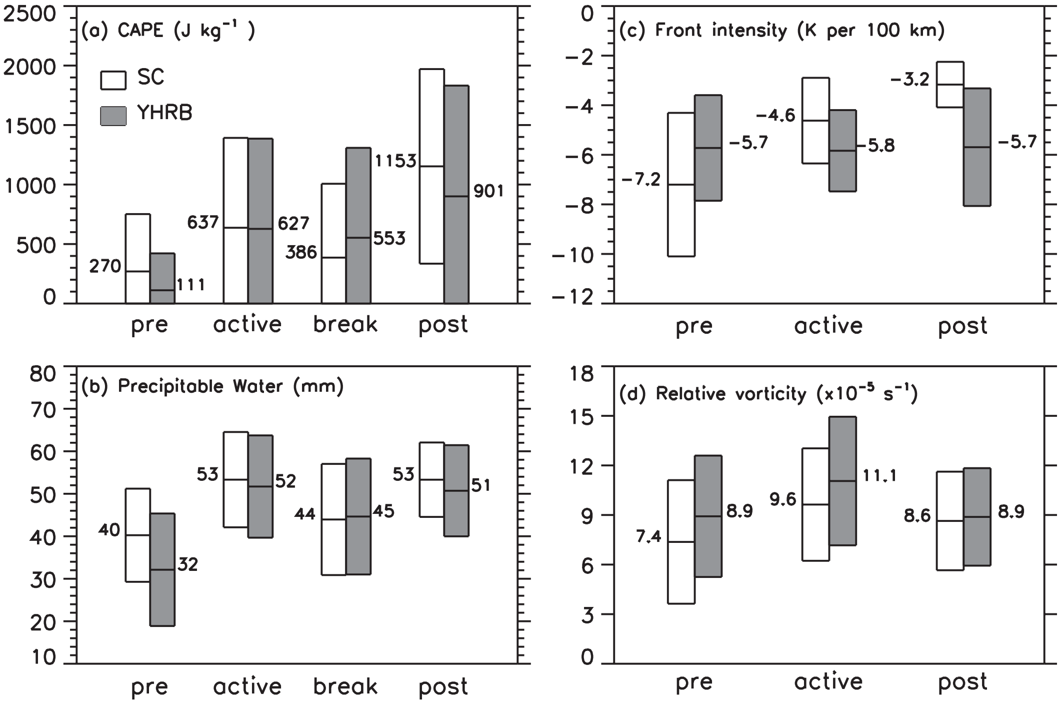

FIG. 7. (a) CAPE, (b) TPW, (c) estimate of front intensity (minimum $\partial\theta_e/\partial y$), and (d) relative vorticity in SC (white bars) and the YHRB (gray bars) during their premonsoon, monsoon active, monsoon break, and postmonsoon periods of 2000–10. (c),(d) The times when TRMM detected the MCS-type PFs. Results for the monsoon break period are not shown in (c),(d) because of the insufficient number of samples. The middle of each bar represents the mean and the top (bottom) of each bar indicates the mean plus (minus) the standard deviation.

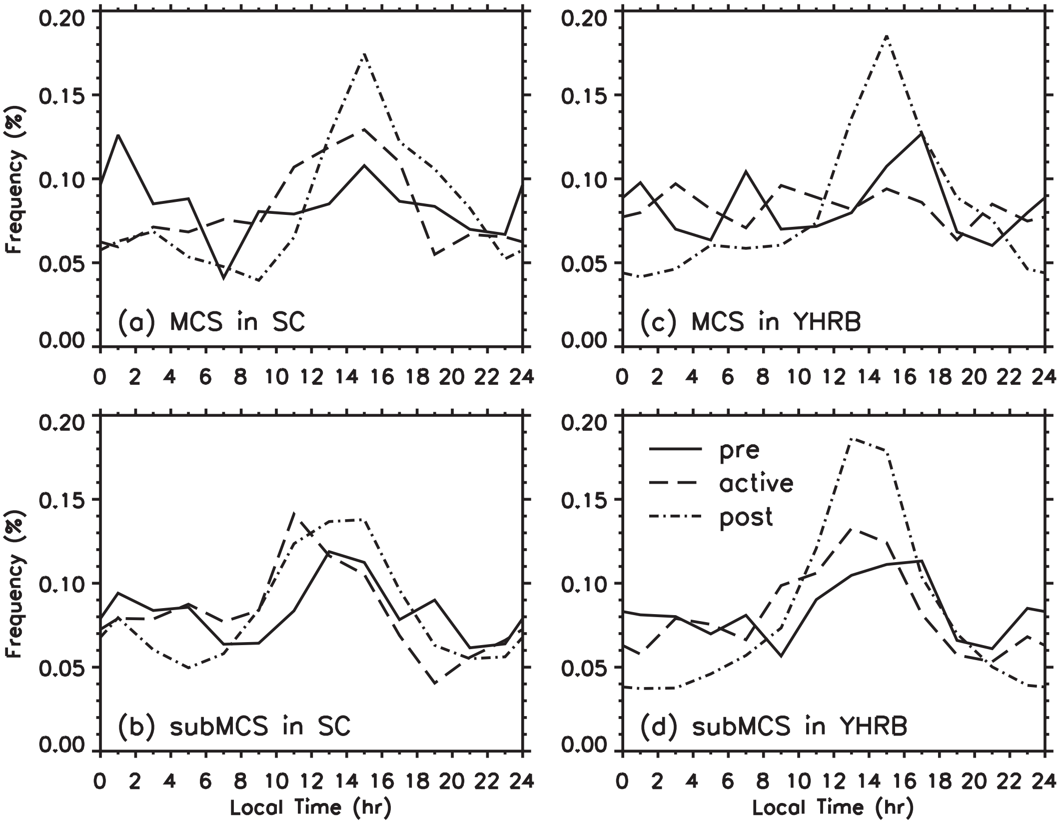

FIG. 8. Diurnal variations of occurrence frequency of the MCS- and sub-MCS-type PFs in (left) SC and (right) the YHRB, during their premonsoon (solid lines), monsoon active (long dashed lines), and postmonsoon (dashed–dotted lines) periods of 1998–2010. Results in the monsoon break period are not shown because of the insufficient number of samples.

period (284 mm), which accounts for 95% of the entire monsoon (300 mm). Those during the premonsoon (203 mm) and postmonsoon (223 mm) are only 71% and 79% of the monsoon active period. While 12.7% of the SC area has a rainfall accumulation >360 mm per season during the monsoon active period, the areal fractions are only 0% and 2.9% in the pre- and postmonsoon periods. The heavy rainfall contribution decreases from 30% (monsoon active period) to 19% (premonsoon) and 29% (postmonsoon). The fraction of area with significant (>50%) heavy rainfall contribution also decreases from 7.0% (monsoon active period) to 1.1% (premonsoon) and 2.3% (postmonsoon).

Contributions to the total population and total near-surface rain from the three PF categories are broadly similar among the periods (Table 4): only 3%–4% of the PF population belongs to the MCS-type that produces about 80%–90% of the total rain amount, whereas only several percentages of the total rainfall are from the abundant nonconvective PF category that accounts for 50% (postmonsoon) to 69% (premonsoon) of the total PF population. However, the postmonsoon period presents some differences, with the largest (smallest) contributions from the sub-MCS-type (other type) PFs among the periods. Moreover, diurnal variations of occurrence of the convective PFs (Fig. 8) in the postmonsoon period present peaks at 1500 local solar time that are more pronounced than those during the premonsoon and monsoon active periods. These results seem to suggest a closer relation between the postmonsoon convective storms and solar-heating instability than in the monsoon active and premonsoon periods. This is related to the significantly less occurrence of major weather systems (e.g., surface front and low-level shear line) during the postmonsoon period, which will be discussed in section 6d.

Systematic changes are observed for convective properties among the different periods. Figures 9a–d show the subseasonal variation of convective intensity in SC from the four proxies of convective intensity for the MCS-type PFs. The means of the first three parameters (maxdbz_6km, maxht_30dB*Z*, and min85PCT) show

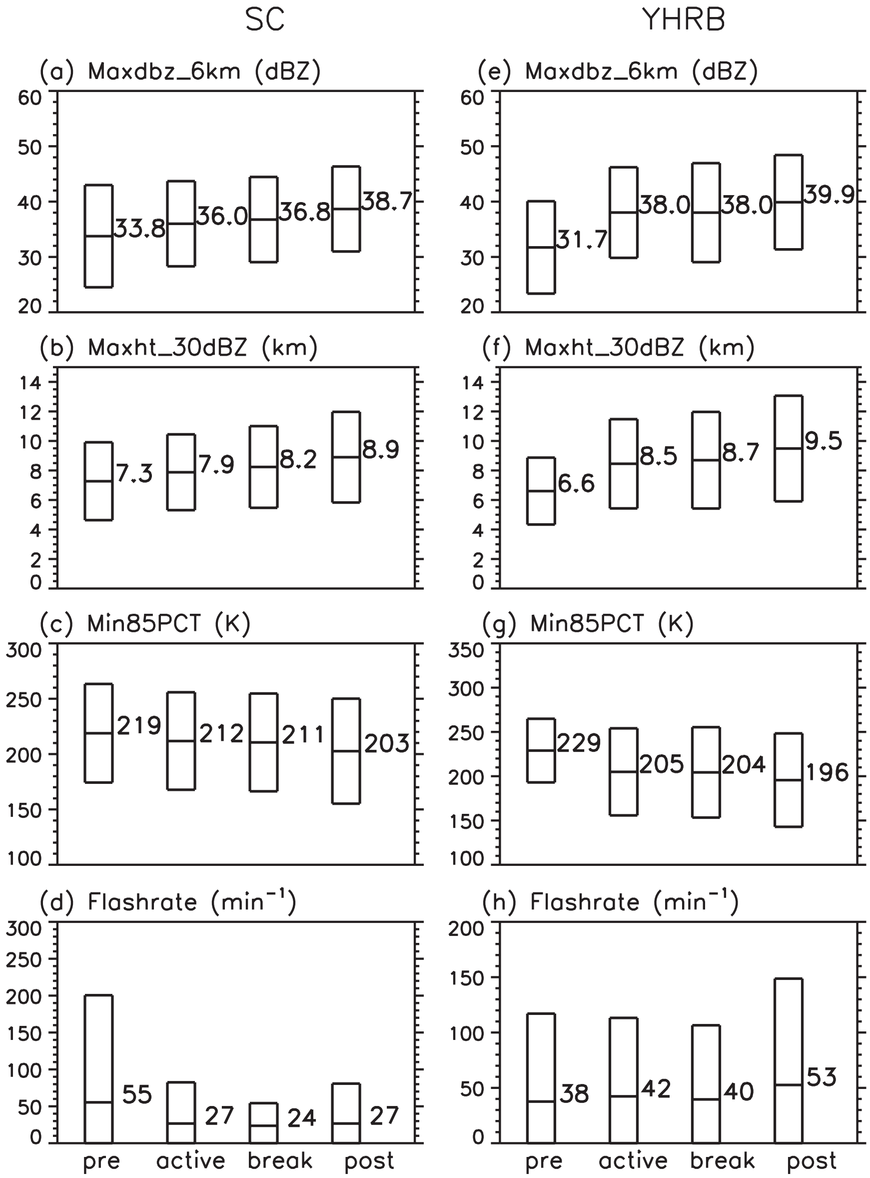

FIG. 9. Proxies of convection intensity of the MCS-type PFs in (left) SC and (right) the YHRB during the premonsoon, monsoon active, monsoon break, and postmonsoon periods of 1998–2010: (a),(e) maximum radar reflectivity at 6 km; (b),(f) maximum height of 30 dBZ; (c),(g) minimum polarization corrected brightness temperature at 85 GHz; and (d),(h) flash rate. The middle of each bar represents the mean and the top (bottom) of each bar indicates the mean plus (minus) the standard deviation. Numbers in each panel represent the mean values for the indicated variables.

consistent intensification of convective activity from the premonsoon to the monsoon and further to the postmonsoon period. However, the mean flash rate in the premonsoon (55 min^{-1}) is about twice of those during the monsoon active and postmonsoon periods (27 min^{-1}) and during the monsoon break period (24 min^{-1}).

The cumulative distributions of VPRR for the MCS-type PF (Figs. 10a–c) show an increase in the echo-top height from the premonsoon to the monsoon and further to the postmonsoon, consistent with the results of the maxdbz_6km, maxht_30dBZ, and min85PCT. At the mixed-phase range of the storms (heights of ~5–10 km), the distribution of radar reflectivity is wider in the premonsoon with more occurrences at the two tails of the distribution relative to the other periods (Figs. 10a–c), which could be related to the larger variation of the flash rates produced by the premonsoon storms (Fig. 9d). The strongest echo at the mixed-phase range of the

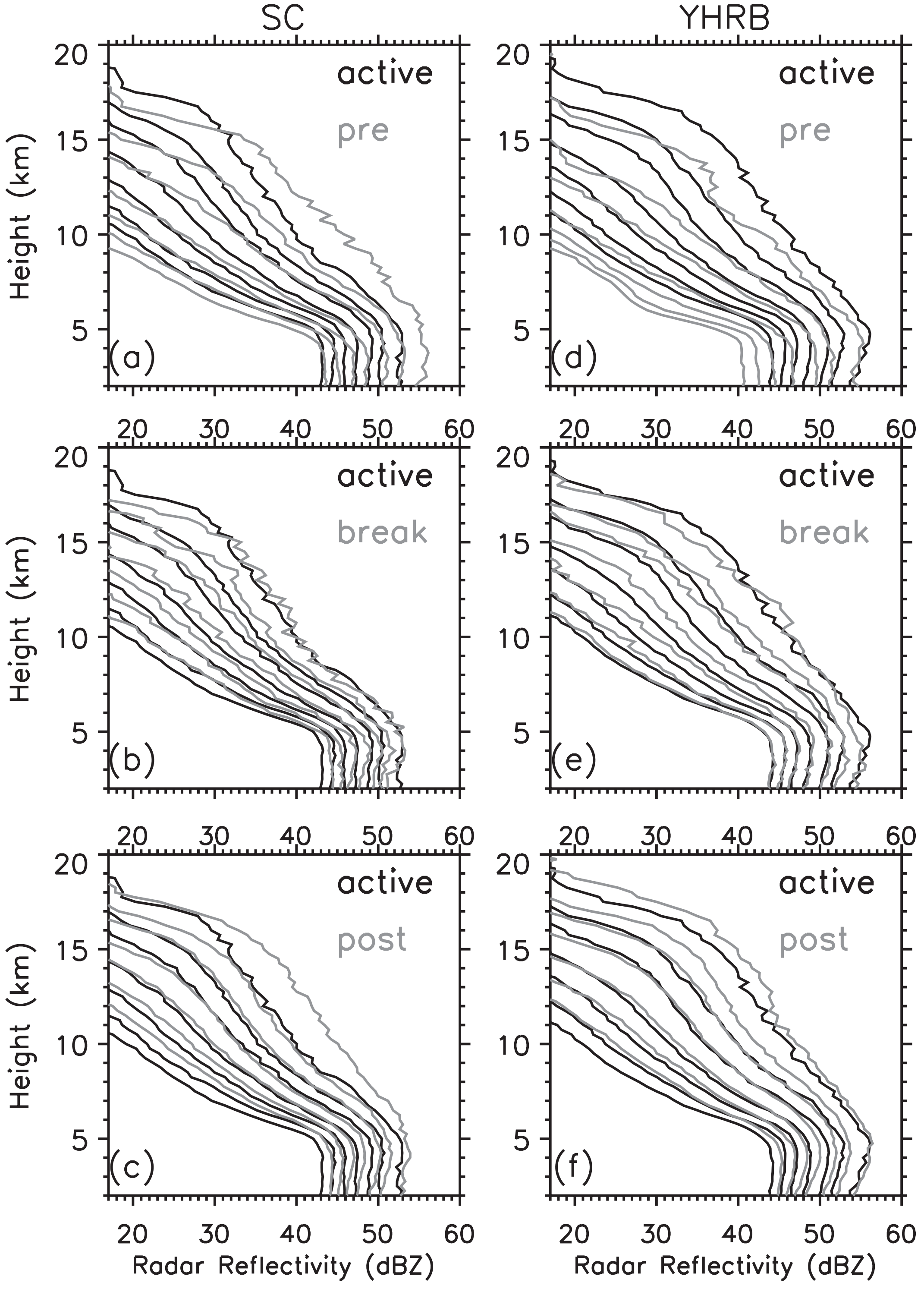

FIG. 10. Cumulative distributions of vertical profiles of maximum radar reflectivity (from bottom to top: in 50th, 60th, 70th, 80th, 90th, 95th, and 99th percentiles) for the MCS-type PFs in the (left) SC and (right) YHRB regions, during the premonsoon, monsoon active, monsoon break, and postmonsoon periods of 1998–2010.

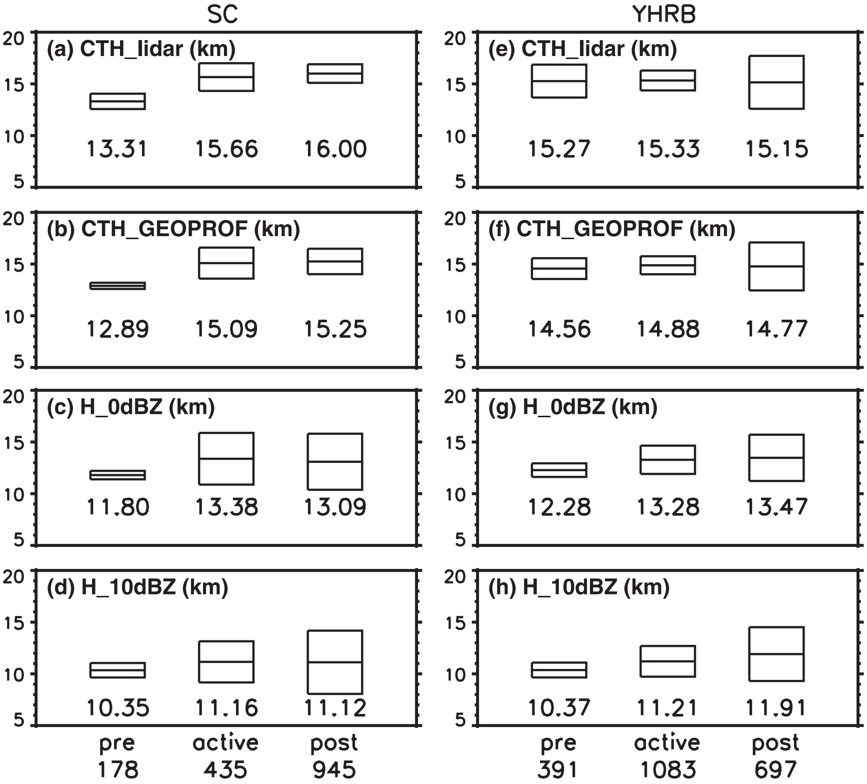

FIG. 11. CTH and ETH of deep convective cores (DCCs) detected by *CloudSat*/*CALIPSO* in (a)–(d) SC and (e)–(h) YRHB, during their premonsoon, monsoon active, and postmonsoon periods of 2006–10. The middle of each bar represents the mean and the top (bottom) of each bar indicates the mean plus (minus) the standard deviation. Numbers in each panel represent the mean values of the CTH or ETH. Numbers shown at the bottom of the figure represent the numbers of the DCC samples. Results during the monsoon break period are not shown because of too few samples of DCSs.

premonsoon storms indicates a larger amount of large-size ice particles, that is, graupel.

b. *Structure of deep convective systems from* CloudSat/CALIPSO

In total, 12, 21, and 39 DCSs were seen by the *CloudSat* over SC during the premonsoon, monsoon active, and postmonsoon periods of 2006–10, within which 178, 435, and 945 DCCs were embedded. Figure 11 provides the mean value and standard deviations of parameters pertaining to the internal vertical structure of deep convection: cloud-top height (CTH) and echo-top height (ETH) of the DCCs. Heights of the DCC tops are comparable between the monsoon active and postmonsoon periods with means of 15.66 and 16.00 km (CTH_lidar) and 15.09 and 15.25 km (CTH_CPR), respectively. They are noticeably higher than those in the premonsoon, where the mean value of CTH_lidar and CTH_CPR is 13.31 and 12.89 km, respectively. For the comparison of ETHs (i.e., H_0dBZ and H_10dBZ), the premonsoon also has substantially lower values (11.80 and 10.35 km) than the monsoon active period (13.38 and 11.16 km) and postmonsoon period (13.09 and 11.12 km). These results, that is, shorter vertical extents of both cloud- and precipitation-size particles in the premonsoon DCCs, suggest weaker deep convection over SC in the premonsoon period relative to the later three periods.

The enhancement of convective intensity from the premonsoon to the monsoon period suggested by *CloudSat* is in broad agreement with the TRMM observations (Figs. 9 and 10). The insignificant contrasts between the monsoon and postmonsoon periods based on the *CloudSat* observations of DCCs are somewhat different from the more notable contrasts based on the TRMM such as maxdbz_6km and maxht_30dBZ (Fig. 9). It should, however, be noted that *CloudSat* CPR (wavelength ~ 3 mm) has higher sensitivity to smaller particles than the TRMM PR (wavelength ~ 2.2 cm) and subsequently the *CloudSat* parameters may measure a different part of the convective system than those of TRMM. Some lack of agreement could also be attributable to smaller sample size and incomplete sampling of the diurnal cycle from the *CloudSat* (Liu et al. 2008b).

Table 6 shows that DCS size is larger during the monsoon active period (279 km) and smaller during the premonsoon (156 km) and postmonsoon (245 km). DCC fractions are 10.5%, 8.2%, and 15.5% from premonsoon to monsoon active to postmonsoon period, respectively, which correspond to 16 km, 23 km, and 38 km. Progressively larger DCC coverage from premonsoon to monsoon active to postmonsoon may be indicative of the increasing convective intensity. Anvil fraction increases from the premonsoon period (42.5%) to the monsoon active and postmonsoon periods (about 57%). However, given the largest DCS size during the monsoon active period, anvil coverage per DCS is also the greatest during that time.

c. *Thermodynamic and dynamic conditions and weather systems*

Along with the subseasonal variation of the eastern Asia atmospheric circulation (Fig. 12), CAPE and TPW over SC increase substantially from the premonsoon to the monsoon and further to the postmonsoon (Figs. 7a,b): The mean values of CAPE in the four periods are 270 (premonsoon), 637 (monsoon active), 386 (monsoon break), and 1153 J kg^{-1} (postmonsoon), while those of TPW are 40, 53, 44, and 53 mm. These subseasonal variations of CAPE and TPW in general agree with that of equivalent potential temperature at 850 hPa (color contours in Figs. 12a–d). The three parameters consistently suggest subsequent increase of convective energy and moisture in the SC environment. Therefore, the subseasonal variations of the atmospheric thermodynamic conditions support the observed subseasonal transitions of the echo-top height, maxdbz_6km, maxht_30dB*Z*, and min85PCT but not the flash rate of the TRMM convective storms.

It is interesting that the monsoon active periods have much smaller values of CAPE but about the same amount of TPW compared to the postmonsoon. The smaller/larger domain-averaged CAPE in the active/postmonsoon periods could be related to the different spatial sizes and lifetime of the precipitation systems during the two periods: the postmonsoon convective storms are smaller (by 60% on average compared to the ones in the monsoon active period) and of shorter lifetime. This explanation is supported by analysis of *CloudSat*/*CALIPSO* data, which shows larger anvil size during the monsoon active period. The much larger horizontal extent of the monsoon rainbands/cloud bands could cool the near-surface air directly through rain evaporation and indirectly by reflecting solar radiation back to outer space and, hence, reducing surface solar heating, both reducing CAPE over a large area. The longer lifetime of the monsoon precipitation systems further enhances the cooling effect, which is accumulated over longer time periods than in the postmonsoon period.

As described previously in section 5d, surface fronts and shear lines in the lower troposphere are the dominant weather systems of the SC storms during the monsoon active period. The concurrent presence of these larger-scale weather systems and the MCS-type PFs (Table 7) occurs 91% of the times in the monsoon active period but decreases to 72% (premonsoon), 52% (monsoon break), and 47% (postmonsoon). The significantly less occurrence of surface fronts and low-level shear lines and the weaker intensity of the fronts during the postmonsoon period (Fig. 7c), along with the more striking afternoon peaks of the postmonsoon convective PFs (Figs. 8a,b), suggests that the precipitation storms are less controlled by the larger-scale weather systems (dynamically driven) but more by local instability due to solar heating (thermodynamically driven). This scale difference of the driving mechanisms can largely explain the differences in the averaged horizontal sizes of storms during the four periods (Table 4): 11 138 km^2 in the monsoon active, 9233 km^2 in the premonsoon, 8189 km^2 in the monsoon break, and 6920 km^2 in the postmonsoon period. These numbers are somewhat smaller than the estimates from *CloudSat*/*CALIPSO* analysis, which can be explained partly by different sensor characteristics and partly by different observing geometries. Nevertheless, both analyses agree that precipitation systems are largest during the monsoon active period.

7. Contrasting monsoon to pre- and postmonsoon periods in the Yangtze and Huai River basins

This section focuses on major similarities and differences between the SC and YHRB regions in the subseasonal variations of precipitation and convection. Minor details are omitted for conciseness.

a. *Surface rainfall accumulation and heavy rainfall contribution*

Both surface rainfall accumulation and heavy rainfall contribution in the YHRB present more significant subseasonal variations than in SC (Table 3). The YHRB region-averaged rainfall accumulations during the pre- and post-mei-yu periods are 135 and 154 mm per season being 54% and 61%, respectively, of the mei-yu active period (252 mm per season). These fractions are smaller than their counterparts in SC: 71% and 79%. The heavy

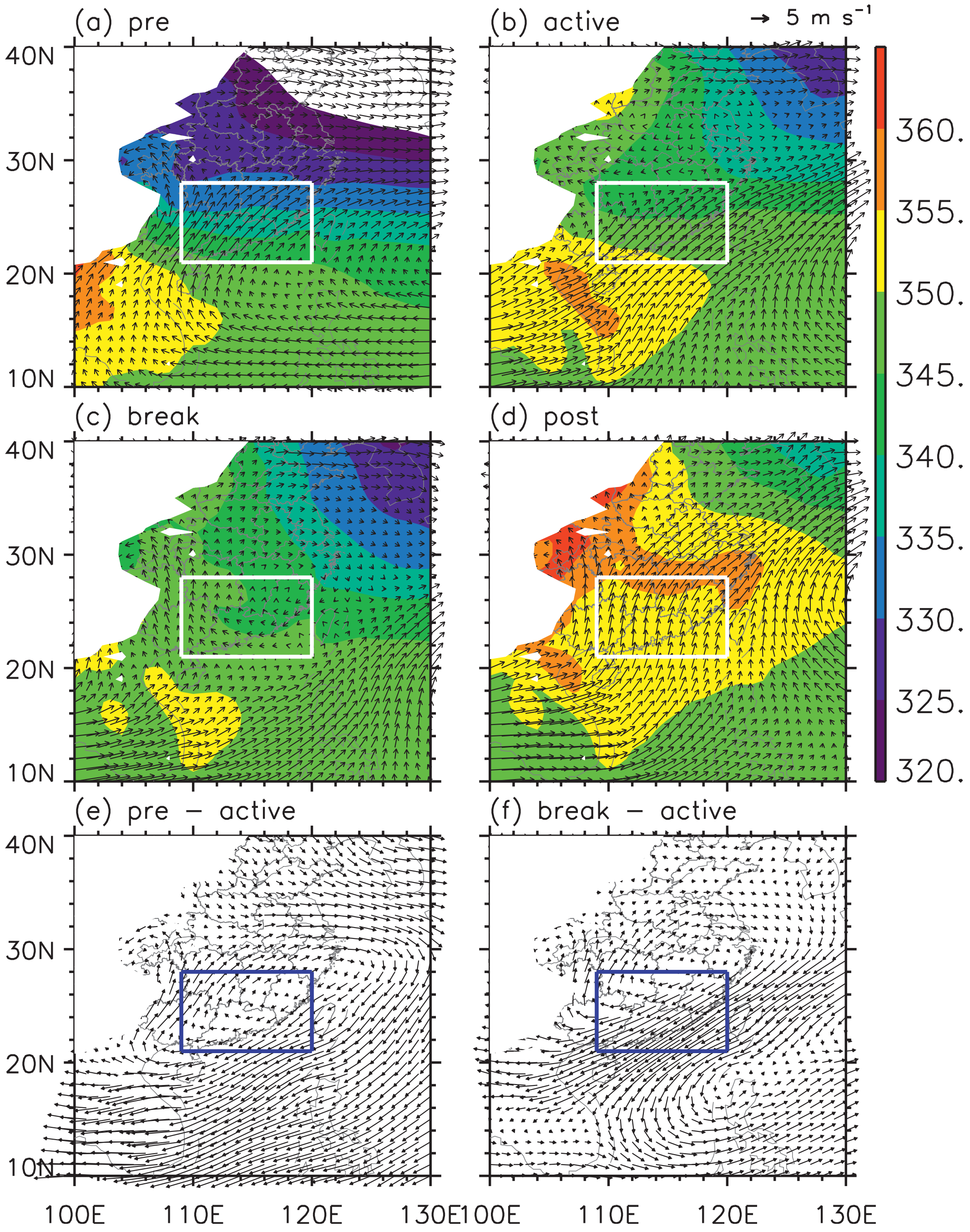

FIG. 12. Equivalent potential temperature and horizontal winds at 850 hPa averaged during the (a) premonsoon, (b) monsoon active, (c) monsoon break, (d) postmonsoon periods of 2000–10 over SC. (e),(f) The differences in horizontal winds between the premonsoon and monsoon active [(a) minus (b)] and between the monsoon break and monsoon active [(c) minus (b)] periods. White lines in (a)–(d) and blue lines in (e),(f) represent boundaries of SC.

rainfall contributions during the pre- and post-mei-yu periods (21% and 20%) are approximately half of the mei-yu active period (38%), while the heavy rainfall contributions over SC during the premonsoon, monsoon active, and postmonsoon periods are closer to each other (19%, 30%, and 29%).

b. *Properties of TRMM PF*

A few similarities are found between the YHRB and SC in terms of subseasonal variations of the statistical properties of the TRMM PFs. First, contributions to total population and rainfall from the three PF categories in the four periods over the YHRB (Table 5) agree broadly with what has been seen over SC (Table 4): (i) a dominant role of the MCS type to total rainfall regardless of <4% population fractions, (ii) larger contribution to rainfall from the sub-MCS type in the break and postmonsoon periods (13% and 16%) relative to the premonsoon and monsoon active periods (~6%), and (iii) abundant nonconvective PFs that produce little rainfall during all periods. Second, as found for the SC region, the mean areal extent of the MCS-type PFs over the YHRB (Table 5) in the post-mei-yu period (7846 km^2) is smaller than those in the mei-yu active and pre-mei-yu periods (13 251 and 14 047 km^2), which is probably in association with the differences in occurrence frequencies and intensity of the surface front and low-level vortices among the periods (Table 7). These weather systems can help the growth and organization of convective clouds to form convective systems on larger scales. Third, occurrences of the postmonsoon storms have more remarkable afternoon peaks than the premonsoon and monsoon active periods (Fig. 8). This, in combination with the less concurrent presence of the larger-scale weather systems, suggests a closer relation of the postmonsoon storms with the solar-heating-originated local instability.

The four proxies of convective intensity (Figs. 9e–h) and cumulative distributions of VPRR (Figs. 10d–f) from the TRMM observations consistently suggest subsequent intensification of convective activity in YHRB from the pre-mei-yu to the mei-yu and further to the post-mei-yu period, with a more significant enhancement of convective intensity from the pre-mei-yu to the mei-yu period than from the mei-yu to the post-mei-yu period.

In contrast to the SC region where the mean flash rate decreases substantially from the premonsoon (55 min^{-1}) to the monsoon periods (break: 24 min^{-1}; active: 27 min^{-1}) (Fig. 9d), the mean flash rate over YHRB increases slightly from the pre-mei-yu (38 min^{-1}) to the mei-yu (break: 40 min^{-1}; active: 42 min^{-1}) (Fig. 9h). Further comparison between the two regions suggests that details in the change of convective intensity from the premonsoon to monsoon active periods may be important. The smaller flash rate during the pre-mei-yu period in the YHRB could be caused by overly too weak convective strength (Figs. 9e–g): for example, the averaged maxht_30dBZ is 6.6 km, being 1.9 km lower than the mei-yu active period (8.5 km). The layer of the storms where high-density graupel collides with low-density ice crystals (which is a key mechanism for charge separation needed for lightning formation; e.g., Takahashi 1978; Saunders 1993) is much shallower in the pre-mei-yu period limiting generation of higher flash rates than the mei-yu period. In contrast, the SC region has more similar convective intensity from the premonsoon to the monsoon period (Fig. 9a–c): the maxht_30dBZ is 7.3 km in the premonsoon period being only 0.6 km lower than the monsoon active one (7.9 km). With more similar convective intensity during the two periods in SC, other factors that can influence lightning production such as aerosol (Sherwood et al. 2006) may have a better chance to stand out. The decreasing (increasing) amount of graupel in the mixed-phase range of the storms from the premonsoon to the monsoon period over the SC (YHRB) region can also be inferred from the VPRR (Fig. 10a versus Fig. 10d). Clearly, more studies are needed to further elucidate the different mechanisms that contribute to the storm electrification.

c. *Structure of deep convective systems from* CloudSat/CALIPSO

The subseasonal variations of convective intensity in the YHRB region based on TRMM are supported by *CloudSat* observations of DCC ETHs (Figs. 11g,h): during the pre-mei-yu, mei-yu active, and post-mei-yu periods, the mean H_0dBZ are 12.27, 13.28, and 13.47 km while those of H_10dBZ are 10.37, 11.21, and 11.91 km. CTHs, on the other hand, do not show significant contrast between the periods, which underlines the difference between the vertical extent of small-size cloud particles (CTH_lidar and CTH_GEOPROF) and precipitation-size particles (H_0dBZ and H_10dBZ).

The anvil fraction out of the DCSs in the YHRB increases from the premonsoon period (40.1%) to the monsoon active and postmonsoon periods (52.3% and 48.9%). This variation is qualitatively similar to SC (Table 6). DCS size is greater during the monsoon active period (176 km) than postmonsoon (159 km). However, a large reading (515 km) is found for the premonsoon period. Small sample sizes (12) may skew the statistics somewhat; nevertheless, we note that TRMM-based MCSs also exhibit the largest size during the premonsoon period over the YHRB region (Table 5).

d. *Thermodynamic and dynamic conditions and weather systems*

Variations of the eastern Asia atmospheric circulation during the four periods of the YHRB region are shown in Fig. 13. Accompanying these variations of atmospheric circulation, thermodynamic conditions of the air over the YHRB change substantially (Fig. 7): the mean values of CAPE for the four periods are 111, 627, 553, and 901 J kg^{-1} and those of TPW are 32, 52, 45, and 51 mm, respectively, which provides the environment supporting the subsequent intensification of convective activity associated with the YHRB storms. These subseasonal changes are generally in agreement with those in SC, as discussed in section 6c, except for the more

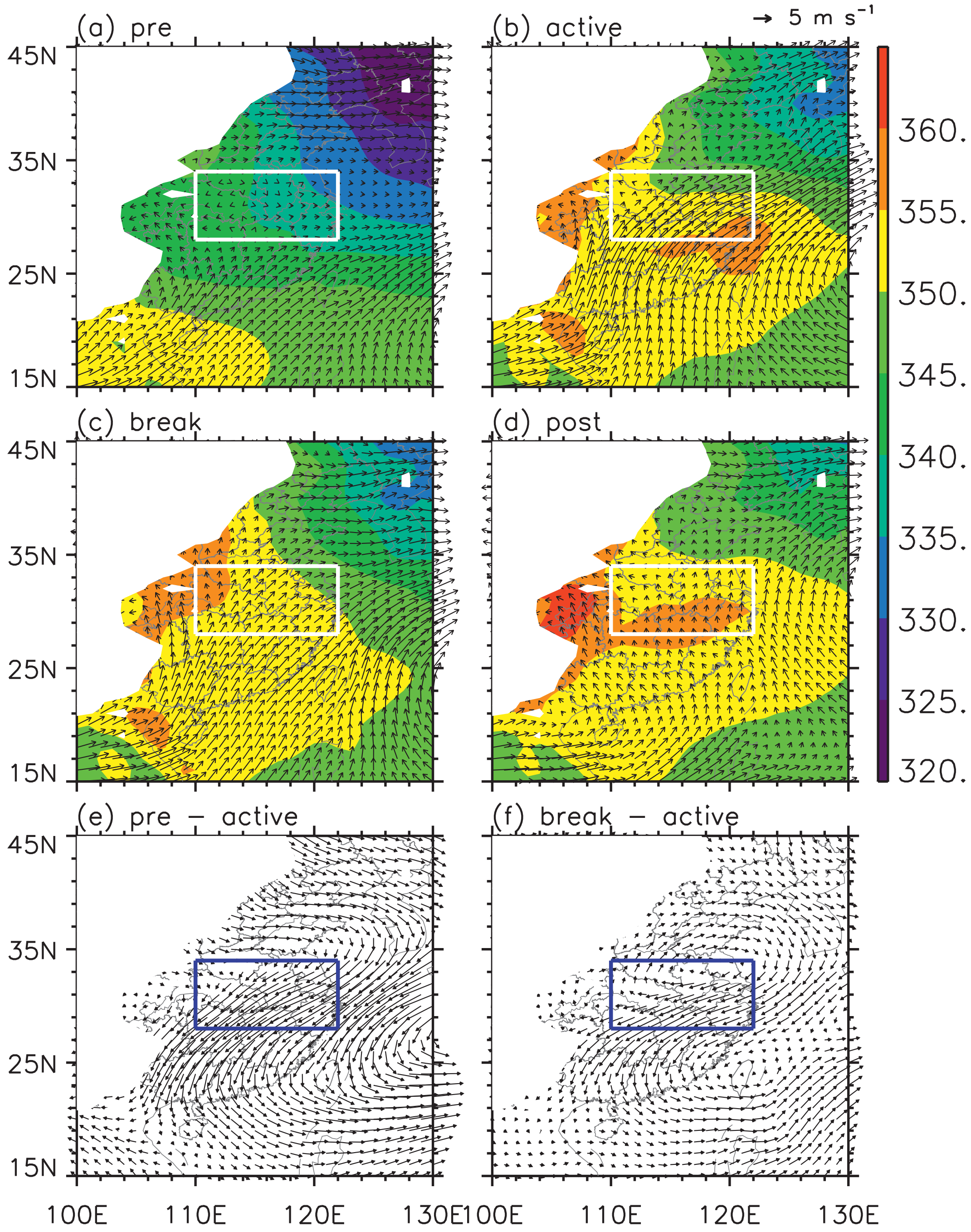

FIG. 13. Equivalent potential temperature and horizontal winds at 850 hPa averaged during the (a) pre-mei-yu, (b) mei-yu active, (c) mei-yu break, and (d) post-mei-yu periods of 2000–10 over the YHRB. (e),(f) The differences in horizontal winds between the pre-mei-yu and mei-yu active [(a) minus (b)] and between the mei-yu break and mei-yu active [(c) minus (b)] periods. White lines in (a)–(d) and blue lines in (e),(f) represent boundaries of the YHRB.

significant variation of convection environment from the pre-mei-yu to the mei-yu period in YHRB.

Surface fronts and/or low-level shear lines were present during 91% of the times of the MCS-type PF over YHRB during the monsoon active period (Table 7). The percentage decreases to 82% (pre-mei-yu), 70% (break), and 64% (post-mei-yu). Similar to what was pointed out previously for SC, the more occurrences of these larger-scale weather systems over YHRB during the mei-yu active and pre-mei-yu periods probably contribute to the larger horizontal spans of the convective storms in the region (Table 5; 14 047 and 13 251 km^2) than those in the break and post-mei-yu periods (8178 and 7864 km^2). Note that the convective systems over the YHRB experience a more concurrent presence of surface fronts than those over SC during their corresponding pre- and postmonsoon periods. Moreover, the concurrent presence of the YHRB vortices is 3 (premonsoon) or 2 times (the other three periods) the corresponding SC ones. The less concurrent presence of weather and precipitation systems in SC are closely related to more mountainous regions in SC than in theYHRB (Fig. 1b) as pointed out previously in section 5d.

8. Summary

Rainfall characteristics and convective properties of the Asian–Pacific summer monsoon precipitation systems have been investigated by a number of investigators (e.g., Islam and Uyeda 2006; Houze et al. 2007; Yuan and Qie 2008; Xu et al. 2009). Our present study builds upon them and focuses on two specific regions that are especially susceptible to severe storms and heavy rainfall during the monsoon/mei-yu period: South China (SC) and the Yangtze–Huai River basin (YHRB) of eastern China. Comparisons are made between the SC and the YHRB regions during their monsoon active periods to reveal variations of monsoonal precipitation systems along with the northward march of the eastern Asian summer monsoon. In each region, the monsoon period is contrasted to the pre- and postmonsoon periods to unveil subseasonal transitions of the precipitation systems, conditions of the environment, and the relevant weather systems. The principal findings of the paper are as follows.

1) Analysis of the new gridded, ground-based daily precipitation dataset shows that, during the monsoon active periods, precipitation over both regions is characterized by extensive rainbands with a nearly west–east orientation and average life period of 5 days. Heavy rainfall ($>$50 mm day^{-1}) contributes significantly to the total monsoon rain accumulation, especially among a few local rainfall centers where the contribution from heavy rainfall exceeds 50%. Region-averaged rain accumulation is greater in SC (284 mm per season) than the YHRB (252 mm per season). However, the heavy rainfall contribution is greater in YHRB.
2) In both regions, MCS-type PFs are the dominant rainfall producer accounting for approximately 90% of the total near-surface rainfall. Convective intensity is compared between the two regions during the monsoon active period using the TRMM data: all four proxies (maxdbz_6km, maxht_30dB*Z*, min85PCT, and flash rate) consistently point to stronger convection in the YHRB, although the SC monsoon storms occur more frequently producing larger total rainfall accumulation.
3) The differences in precipitation characteristics and convective properties between SC and YHRB are closely related to the topographic features, environmental atmospheric conditions and major weather systems in these regions. The stronger convection in the YHRB during the monsoon active period is found to coincide with higher concurrent presence and stronger intensity of the surface front and lower-level vortex in that region. On the other hand, the more frequent occurrence of precipitation systems and larger rainfall accumulation in SC can be traced to the more mountainous land and closer proximity to the ocean.
4) All convection proxies (except for lightning flash rate) suggest that convection in both regions intensifies progressively from the premonsoon to the monsoon and further to the postmonsoon period, with more significant enhancement of convective strength from the premonsoon to the monsoon period in the YHRB. These subseasonal variations of convective intensity are largely in agreement with those of the convective available potential energy (CAPE) and total precipitable water, which results from the subseasonal variations of the large-scale atmospheric circulation.
5) Lightning flash rate decreases substantially from the premonsoon to the monsoon period at SC but increases slightly from the pre-mei-yu to the mei-yu period in the YHRB. The opposite trends in flash rate over SC and YHRB may be related to variations in convective intensity, which is more similar between the premonsoon period and the monsoon period in SC, but exhibits a significant jump from the pre-mei-yu to mei-yu in YHRB. These results suggest that more studies are needed concerning the roles of convective dynamics and other factors (e.g., aerosols) in determining the storm lightning associated with the EASM.
6) There is a scale difference in the driving mechanisms for rainfall production during the four periods (premonsoon, monsoon active, monsoon break, and postmonsoon) over both SC and YHRB: the precipitation systems are less controlled by larger-scale weather systems (dynamically driven) but more by local instability due to solar heating (thermodynamically driven) during the postmonsoon and monsoon break periods. This scale difference can largely explain the smaller horizontal extents of the precipitation systems

in the postmonsoon and monsoon break periods. It can also contribute to the more pronounced afternoon peaks in the diurnal cycles of the occurrence of the postmonsoon convective storms.

Acknowledgments. This research is jointly supported by the National Basic Research Program of China (973 Program; 2012CB417202), the National Natural Science Foundation of China (Projects 41175049 and 40921003), the National Key Technology R&D Program of China (2012BAC22B03), and the Basic Research Fund of the Chinese Academy of Meteorological Sciences (CAMS) (2012Y001). Dr. Z. Luo acknowledges supports from NASA under Grant NNX10AM31G and NNX12AC13G. We also acknowledge the National Meteorological Center of the China Meteorological Administration for providing the weather maps. We thank Drs. Edward Zipser and Chuntao Liu at University of Utah for the help on using the TRMM data. Thanks are also given to our colleagues Tao Niu and Min Wen, respectively, for providing the gridded daily rainfall product and helpful discussions. The NCEP FNL data were obtained from the Research Data Archive (RDA), which is maintained by the Computational and Information Systems Laboratory at the National Center for Atmospheric Research (NCAR).

REFERENCES

Arakawa, A., 2004: The cumulus parameterization problem: Past, present, and future. *J. Climate,* **17,** 2493–2525.

Awaka, J., T. Iguchi, and K. Okamoto, 1998: Early results on rain type classification by the Tropical Rainfall Measuring Mission (TRMM) precipitation radar. *Proc. Eighth Open Symp. on Wave Propagation and Remote Sensing,* Aveiro, Portugal, URSI Commission F, 143–146.

Barnes, S. L., 1964: A technique for maximizing details in a numerical weather map analysis. *J. Appl. Meteor.,* **3,** 396–409.

Cecil, D. J., E. J. Zipser, and S. W. Nesbitt, 2002: Reflectivity, ice scattering, and lightning characteristics of hurricane eyewalls and rainbands. Part I: Quantitative description. *Mon. Wea. Rev.,* **130,** 769–784.

——, S. J. Goodman, D. J. Boccippio, E. J. Zipser, and S. W. Nesbitt, 2005: Three years of TRMM precipitation features. Part I: Radar, radiometric, and lightning characteristics. *Mon. Wea. Rev.,* **133,** 543–566.

Chang, C.-P., Y. Ding, N.-C. Lau, R. H. Johnson, B. Wang, and T. Yasunari, 2010: *The Global Monsoon System: Research and Forecast.* Series on Asia-Pacific Weather and Climate, Vol. 5, World Scientific, 594 pp.

Chen, G. T.-J., 1988: On the synoptic climatological characteristics of the East Asian Meiyu front (in Chinese with English abstract). *Atmos. Sci.,* **16,** 435–446.

Ding, Y. H., 2007: The variability of the Asian summer monsoon. *J. Meteor. Soc. Japan,* **85B,** 21–54.

——, and Y. J. Liu, 2001: Onset and the evolution of the summer monsoon over south China during SCSMEX field experiment in 1998. *J. Meteor. Soc. Japan,* **79,** 367–380.

——, and J. C. L. Chan, 2005: The East Asian summer monsoon: An overview. *Meteor. Atmos. Phys.,* **89,** 117–142.

——, Y. Zhang, Q. Ma, and G. Q. Hu, 2001: Analysis of the large-scale circulation features and synoptic systems in East Asia during the intensive observation period of GAME/HUBEX. *J. Meteor. Soc. Japan,* **79,** 277–300.

——, Y. Y. Liu, L. Zhang, J. J. Liu, L. Zhao, and Y. F. Song, 2011: The Meiyu weather system in East Asia: Build-up, maintenance and structures. *The Global Monsoon System: Research and Forecast.* 2nd ed. Chih-Pei Chang et al., Eds., World Scientific, 205–221.

Fujinami, H., and T. Yasunari, 2009: The effects of midlatitude waves over and around the Tibetan Plateau on submonthly variability of the East Asian summer monsoon. *Mon. Wea. Rev.,* **137,** 2286–2304.

Houze, R. A., Jr., D. C. Wilton, and B. F. Smull, 2007: Monsoon convection in the Himalayan region as seen by the TRMM precipitation radar. *Quart. J. Roy. Meteor. Soc.,* **133,** 1389–1411.

Hu, J.-L., R.-H. Zhang, and T. Niu, 2008: A daily precipitation grid dataset with 0.1° resolution in Changjiang River valley and its precision (in Chinese). *J. Nat. Res.,* **23,** 136–148.

Hu, Y.-M., and Y.-H. Ding, 2010: Simulation of 1991−2005 Meiyu seasons in the Yangtze-Huaihe region using BCC_RegCM 1.0. *Chin. Sci. Bull.,* **55,** 1077–1083.

——, ——, and F. Liao, 2008: A study of updated definition and climatological characters of Meiyu season in the Yangtze-Huaihe region. *Chin. J. Atmos. Sci,* **32,** 101–112.

Iguchi, T., T. Kozu, R. Meneghin, J. Awaka, and K. Okamoto, 2000: Rain-profiling algorithm for the TRMM precipitation radar. *J. Appl. Meteor.,* **39,** 2038–2052.

Islam, M. N., and H. Uyeda, 2006: TRMM observed vertical structure and diurnal variation of precipitation in South Asia. *Proc. Int. Geoscience and Remote Sensing Symp.,* Denver, CO, IEEE, 1292–1295.

Jin, R. H., M. Y. Jiao, J. Xu, and H. F. Qin, 2006: Abnormal characteristics and causes analysis of the western Pacific subtropical high activity during the Huaihe floods in 2003 (in Chinese). *J. Trop. Meteor.,* **22,** 60–66.

Kalnay, E., and Coauthors, 1996: The NCEP/NCAR 40-Year Reanalysis Project. *Bull. Amer. Meteor. Soc.,* **77,** 437–471.

Kummerow, C., W. Barnes, T. Kozu, J. Shiue, and J. Simpron, 1998: The Tropical Rainfall Measuring Mission (TRMM) sensor package. *J. Atmos. Oceanic Technol.,* **15,** 809–817.

Li, L., R. Zhang, and M. Wen, 2011: Diagnostic analysis of the evolution mechanism of a vortex over the Tibetan Plateau in June 2008. *Adv. Atmos. Sci.,* **28,** 797–808.

Liang, P., and Y. Ding, 2011: Does non-occurrence of Meiyu rake place in Yangtze-Huaihe basins during summer of 2009? (in Chinese with English abstract).*Plateau Meteor.,* **30,** 53–64.

Liu, C., 2007: University of Utah TRMM precipitation and cloud feature database: Description version 1.0. University of Utah Department of Meteorology Rep., 22 pp. [Available online at http://trmm.chpc.utah.edu/docs/trmm_database_description_v1.0.pdf.]

——, E. J. Zipser, D. J. Cecil, S. W. Nesbitt, and S. Sherwood, 2008a: A cloud and precipitation feature database from nine years of TRMM observations. *J. Appl. Meteor. Climatol.,* **47,** 2712–2728.

——, ——, G. G. Mace, and S. Benson, 2008b: Implications of the differences between daytime and nighttime CloudSat observations over the tropics. *J. Geophys. Res.,* **113,** D00A04, doi:10.1029/2008JD009783.

Luo, Y., Y. Wang, H. Wang, Y. Zheng, and H. Morrison, 2010: Modeling convective-stratiform precipitation processes on a Mei-Yu front with the Weather Research and Forecasting model: Comparison with observations and sensitivity to cloud microphysics parameterizations. *J. Geophys. Res.,* **115,** D18117, doi:10.1029/2010JD013873.

——, R. Zhang, W. Qian, Z. Luo, and X. Hu, 2011: Intercomparison of deep convection over the Tibetan Plateau–Asian monsoon region and subtropical North America in boreal summer using CloudSat/CALIPSO data. *J. Climate,* **24,** 2164–2177.

Mace, G. G., R. Marchand, Q. Zhang, and G. Stephens, 2007: Global hydrometeor occurrence as observed by CloudSat: Initial observations from summer 2006. *Geophys. Res. Lett.,* **34,** L09808, doi:10.1029/2006GL029017.

Mao, J. Y., and G. X. Wu, 2006: Intraseasonal variations of the Yangtze rainfall and its related atmospheric circulation features during the 1991 summer. *Climate Dyn.,* **27,** 815–830.

Mapes, B. E., and R. A. Houze Jr., 1995: Diabatic divergence profiles in western Pacific mesoscale convective systems. *J. Atmos. Sci.,* **52,** 1807–1828.

Medina, S., R. A. Houze, A. Kumar, and D. Niyogi, 2010: Summer monsoon convection in the Himalayan region: Terrain and land cover effects. *Quart. J. Roy. Meteor. Soc.,* **136,** 593–616.

Nesbitt, S. W., E. J. Zipser, and D. J. Cecil, 2000: A census of precipitation features in the tropics using TRMM: Radar, ice scattering, and lightning observations. *J. Climate,* **13,** 4087–4106.

Ninomiya, K., 2004: Large- and mesoscale features of meiyu-baiu front associated with intense rainfalls. *East Asian Monsoon,* C. P. Chang, Series on Asia-Pacific Weather and Climate, Vol. 5, World Scientific, 404–435.

——, and Y. Shibagaki, 2007: Multi-scale features of the meiyu-baiu front and associated precipitation systems. *J. Meteor. Soc. Japan,* **85B,** 103–122.

Romatschke, U., and R. A. Houze, 2011: Characteristics of precipitating convective systems in the South Asian monsoon. *J. Hydrometeor.,* **12,** 3–26.

Saunders, C. P. R., 1993: A review of the thunderstorm electrification processes. *J. Appl. Meteor.,* **32,** 624–655.

Shen, S. S. P., P. Dzikowski, G. Li, and D. Griffith, 2001: Interpolation of 1961–97 daily climate data onto Alberta polygons of ecodistrict and soil landscape of Canada. *J. Appl. Meteor.,* **40,** 2162–2177.

——, H. Yin, K. Cannon, A. Howard, S. Chetner, and T. R. Karl, 2005: Temporal and spatial changes of the agroclimate in Alberta, Canada, from 1901 to 2002. *J. Appl. Meteor.,* **44,** 1090–1105.

Sherwood, S. C., V. T. J. Phillips, and J. S. Wettlaufer, 2006: Small ice crystals and the climatology of lightning. *Geophys. Res. Lett.,* **33,** L05804, doi:10.1029/2005GL025242.

Stephens, G. L., and Coauthors, 2002: The CloudSat mission and the A-Train. *Bull. Amer. Meteor. Soc.,* **83,** 1771–1790.

——, and Coauthors, 2008a: CloudSat mission: Performance and early science after the first year of operation. *J. Geophys. Res.,* **113,** D00A18, doi:10.1029/2008JD009982.

——, S. van den Heever, and L. Pakula, 2008b: Radiative–convective feedbacks in idealized states of radiative–convective equilibrium. *J. Atmos. Sci.,* **65,** 3899–3916.

Sun, J. H., X. L. Zhang, L. L. Qi, and S. X. Zhao, 2005: An analysis of a meso-β-system in a mei-yu front using the intensive observation data during CHeRES 2002. *Adv. Atmos. Sci.,* **22,** 278–289.

Takahashi, T., 1978: Riming electrification as a charge generation mechanism in thunderstorms. *J. Atmos. Sci.,* **35,** 1536–1548.

Varble, A., and Coauthors, 2011: Evaluation of cloud-resolving model intercomparison simulations using TWP-ICE observations: Precipitation and cloud structure. *J. Geophys. Res.,* **116,** D12206, doi:10.1029/2010JD015180.

Wang, J., J. He, X. Liu, and B. Wu, 2008: Interannual variability of the Meiyu onset over Yangtze-Huaihe River valley and analyses of its previous strong influence signal. *Chin. Sci. Bull.,* **54,** 687–695.

Xie, A., Y. Chung, X. Liu, and Q. Ye, 1998: The interannual variations of the summer monsoon onset over the South China Sea. *Theor. Appl. Climatol.,* **59,** 201–213.

Xu, W., E. J. Zipser, and C. Liu, 2009: Rainfall characteristics and convective properties of mei-yu precipitation systems over South China, Taiwan, and the South China Sea. Part I: TRMM observations. *Mon. Wea. Rev.,* **137,** 4261–4275.

Yang, J., B. Wang, B. Wang, and Q. Bao, 2010: Biweekly and 21–30-day variations of the subtropical summer monsoon rainfall over the lower reach of the Yangtze River basin. *J. Climate,* **23,** 1146–1159.

Yasunari, T., and T. Miwa, 2006: Convective cloud systems over the Tibetan Plateau and their impact on meso-scale disturbances in the meiyu/baiu frontal zone—A case study in 1998. *J. Meteor. Soc. Japan,* **84,** 783–803.

Yu, R., T. Zhou, A. Xiong, Y. Zhu, and J. Li, 2007: Diurnal variations of summer precipitation over contiguous China. *Geophys. Res. Lett.,* **34,** L01704, doi:10.1029/2006GL028129.

Yuan, T., and X. Qie, 2008: Study on lightning activity and precipitation characteristics before and after the onset of the South China Sea summer monsoon. *J. Geophys. Res.,* **113,** D14101, doi:10.1029/2007JD009382.

Zhao, Y., Z. Li, and Z. Xiao, 2008: A diagnostic and numerical study on a rainstorm in South China influenced by a northward-propagating tropical system. *Acta Meteor. Sin.,* **22,** 284–302.

Zhao, Z. G., 1999: *Summer Drought/Flood and Their Environmental Fields in China* (in Chinese). China Meteorological Press, 10 pp.

Zipser, E. J., and K. R. Lutz, 1994: The vertical profile of radar reflectivity of convective cells: A strong indicator of storm intensity and lightning probability? *Mon. Wea. Rev.,* **122,** 1751–1759.

——, D. J. Cecil, C. Liu, S. W. Nesbitt, and D. Yorty, 2006: Where are the most intense thunderstorms on Earth? *Bull. Amer. Meteor. Soc.,* **87,** 1057–1071.